

BUT FILE COPY

(4)

GI-TR-90-0012

AD-A222 185

Frequency Dependent Attenuation in Rocks

Karl B. Coyner
Randolph J. Martin, III

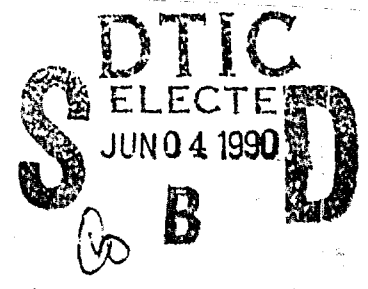
New England Research Inc
76 Olcott Drive
White River Jct, VT 05001

20 January 1990

Final Report
3 September 1987-2 September 1989

APPROVED FOR PUBLIC RELEASE; DISTRIBUTION UNLIMITED

GEOPHYSICS LABORATORY
AIR FORCE SYSTEMS COMMAND
UNITED STATES AIR FORCE
HANSCOM AIR FORCE BASE, MASSACHUSETTS 01731-5000



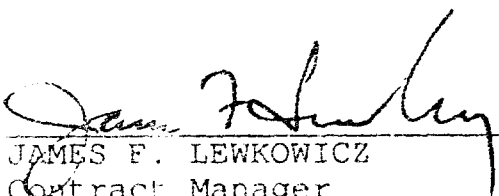
90 05 31 065

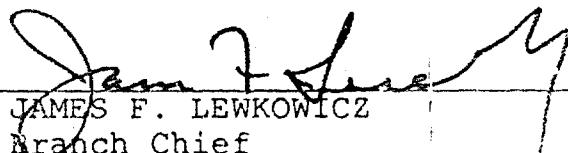
SPONSORED BY
Defense Advanced Research Projects Agency
Nuclear Monitoring Research Office
ARPA ORDER NO 5307

MONITORED BY
Geophysics Laboratory
F19628-87-C-0214


The views and conclusions contained in this document are those of the authors and should not be interpreted as representing the official policies, either expressed or implied, of the Defense Advanced Research Projects Agency or the U.S. Government.

This technical report has been reviewed and is approved for publication.


JAMES F. LEWKOWICZ
Contract Manager
Solid Earth Geophysics Branch
Earth Sciences Division


JAMES F. LEWKOWICZ
Branch Chief
Solid Earth Geophysics Branch
Earth Sciences Division

FOR THE COMMANDER


DONALD H. ECKHARDT, Director
Earth Sciences Division

This report has been reviewed by the ESD Public Affairs Office (PA) and is releasable to the National Technical Information Service (NTIS).

Qualified requestors may obtain additional copies from the Defense Technical Information Center. All others should apply to the National Technical Information Service.

If your address has changed, or if you wish to be removed from the mailing list, or if the addressee is no longer employed by your organization, please notify GL/IMA, Hanscom AFB, MA 01731-5000. This will assist us in maintaining a current mailing list.

Do not return copies of this report unless contractual obligations or notices on a specific document requires that it be returned.

Unclassified

SECURITY CLASSIFICATION OF THIS PAGE

REPORT DOCUMENTATION PAGE				Form Approved OMB No 0704-0188	
1a REPORT SECURITY CLASSIFICATION Unclassified			1b RESTRICTIVE MARKINGS		
2a SECURITY CLASSIFICATION AUTHORITY			3 DISTRIBUTION/AVAILABILITY OF REPORT Approved for public release; Distribution unlimited		
2b DECLASSIFICATION/DOWNGRADING SCHEDULE					
4 PERFORMING ORGANIZATION REPORT NUMBER(S)			5 MONITORING ORGANIZATION REPORT NUMBER(S) GL-TR-90-0012		
6a NAME OF PERFORMING ORGANIZATION New England Research Inc		6b OFFICE SYMBOL (If applicable)		7a NAME OF MONITORING ORGANIZATION Geophysics Laboratory	
6c ADDRESS (City, State, and ZIP Code) 76 Olcott Drive White River Jct, VT 05001			7b ADDRESS (City, State, and ZIP Code) Hanscom AFB, MA 01731-5000		
8a NAME OF FUNDING SPONSORING ORGANIZATION		8b OFFICE SYMBOL (If applicable)		9 PROCUREMENT INSTRUMENT IDENTIFICATION NUMBER F19628-87-C-0214	
3c ADDRESS (City, State, and ZIP Code)			10 SOURCE OF FUNDING NUMBERS		
			PROGRAM ELEMENT NO 62714E	PROJECT NO 7A10	TASK NO DA
			WORK UNIT ACCESSION NO DA		
11 TITLE (Include Security Classification) Frequency Dependent Attenuation in Rocks					
12 PERSONAL AUTHOR(S) Karl B. Coyner, Randolph J. Martin, III					
13a TYPE OF REPORT Final		13b TIME COVERED FROM 9/3/87 TO 9/2/89		14 DATE OF REPORT (Year, Month, Day) 1990 January 20	
15 PAGE COUNT 60					
16 SUPPLEMENTARY NOTATION					
17 COSATI CODES			18 SUBJECT TERMS (Continue on reverse if necessary and identify by block number)		
FIELD	GROUP	SUB GROUP	Attenuation		
			Rock Properties		
		Interpreting	(1/2)		
19 ABSTRACT (Continue on reverse if necessary and identify by block number)					
<p>An inconsistency in the interpretation of experimental stress-strain data for attenuation determinations is investigated. Attenuation (Q^{-1}) calculated from the integrated areas of plotted hysteresis loops depend on the definition of maximum strain energy. If maximum strain energy is taken as the entire area under the loading segment of the hysteresis loop, the resulting Q^{-1} are approximately 4 times less than the Q^{-1} from the phase angle ϕ measured between cycled stress and strain ($Q^{-1} = \tan \phi$). This inconsistency is resolved by locating the origin of zero stress and strain at the center of the hysteresis loop, regardless of the absolute sign of stresses and strains, and calculating the maximum strain energy during one cycle relative to that origin. Attenuation calculated from the ratio of hysteresis loop areas must be carefully interpreted before application to seismic wave propagation. \rightarrow</p> <p style="text-align: right;">$\gamma + x < \text{the } 1/6$</p>					
20 DISTRIBUTION/AVAILABILITY OF ABSTRACT <input type="checkbox"/> UNCLASSIFIED/UNLIMITED <input type="checkbox"/> SAME AS RPT. <input type="checkbox"/> DTIC USERS			21 ABSTRACT SECURITY CLASSIFICATION Unclassified		
22a NAME OF RESPONSIBLE INDIVIDUAL James Lewkowicz			22b TELEPHONE (Include Area Code)		22c OFFICE SYMBOL GL/LWH

19. Abstract

Attenuation and dynamic moduli measurements on intact Sierra White granite samples were performed utilizing three experimental techniques: hysteresis loop, resonant bar, and ultrasonic spectral ratio. Extensional attenuations (Q_e^{-1}) and Young's moduli were measured at 0.1 Hz with the hysteresis loop and between 10 and 210 kHz with the resonant bar techniques. Ultrasonic P and S wave velocities and spectral ratio compressional (Q_p^{-1}) and shear (Q_s^{-1}) attenuations were measured in the 100-200 kHz and 0.6 - 1.1 MHz frequency bands, then converted into comparable extensional attenuations and Young's moduli. Compressional velocities and attenuations were also measured at 40-80 kHz. Both room dry and water saturated samples were investigated with all three techniques, and ultrasonic measurements at 0.6 - 1.1 MHz were conducted as a function of confining pressure to 100 MPa.

The Young's moduli for room dry samples are approximately the same (~34 to 35 MPa) at all frequencies, and the hysteresis loop and resonant bar Q_e^{-1} 's are small and comparable to within experimental error (~0.008 to 0.006). The attenuation mechanism is related to small amounts of water adsorbed onto the surfaces of microcracks. In contrast, ultrasonic Q^{-1} 's for room dry samples are much larger and increase quite rapidly with increasing frequency between the three different ultrasonic frequency bands. Between 100 and 200 kHz spectral ratio attenuations ($Q_e^{-1} = 0.024$) are approximately 3 times larger than resonant bar attenuations ($Q_e^{-1} = 0.0053$). A scattering attenuation mechanism for ultrasonic pulses is suggested by these observations.

Water saturation dramatically increases the hysteresis loop and resonant bar Q_e^{-1} 's by factors of 3 and 7.5, respectively, but has a minimal effect on Young's modulus. In contrast, the 0.6 - 1.1 MHz ultrasonic data reveal that Young's modulus nearly doubles while Q_e^{-1} only increases from 0.058 to 0.075. The 0.6 - 1.1 MHz compressional attenuation Q_p^{-1} actually decreases upon saturation, from 0.065 to 0.046, while the 40-80 kHz Q_p^{-1} increases from 0.020 to 0.064. The reduction of attenuation at the higher frequencies provides additional evidence of scattering; scattering cross-sections are reduced when fluid is introduced. The large increase in saturated modulus reflects the unrelaxed dynamic response of pore fluid at ultrasonic frequencies. Attenuation is enhanced at lower frequencies by a dynamic viscous fluid flow mechanism. A relaxation peak in the attenuation spectrum below approximately 10 kHz is indicated by decreasing resonant bar Q_e^{-1} 's as a function of increasing frequency to 90 kHz.

Table of Contents

Summary	1
The Definition and Calculation of Q^{-1} in Hysteresis Loop Attenuation Measurements.....	3
Comparison of Hysteresis Loop, Resonant Bar, and Ultrasonic Attenuation Measurements on Sierra White granite.....	16



Accession For	
NTIS GRA&I	<input checked="" type="checkbox"/>
DTIC TAB	<input type="checkbox"/>
Unannounced	<input type="checkbox"/>
Justification	
By _____	
Distribution/	
Availability Codes	
Dist	Avail and/or Special
A-1	

Summary

In order to clarify the frequency dependence of attenuation between 0.1 and 100 Hz, there is a useful role for laboratory investigations of frequency, strain amplitude, pressure, saturation, and lithology effects. If the laboratory properties of rock can match seismic observations of both the value of Q and its frequency dependence, particularly in the 1 to 20 Hz band, then seismic observations can be interpreted by physical mechanisms quantified through a series of additional experiments. If not, appropriate explanations must rely on other physical realities, such as contrasts in lithology, anisotropy, the presence of fractures, or scattering due to other inhomogeneities.

In many ways the best technique for attenuation and moduli determinations is the hysteresis loop technique. The seismic frequency band can be matched exactly, sample sizes can be adjusted to include inhomogeneities and fractures, and the strain amplitude dependence of attenuation to very large strains may be investigated. The first paper of this report investigates the manner in which hysteresis loop stress-strain data is analyzed for Q^{-1} determination. An inconsistency was discovered in the attenuation definition $Q^{-1} = \delta W / 2\pi W$, where δW is the dissipated energy, or the area of the hysteresis loop, and W is the maximum strain energy introduced into the sample during one cycle, or the area under the increasing load portion of the loop. The inconsistency often results in Q^{-1} that is a factor of four times less than the equivalent phase angle attenuation, $Q^{-1} = \tan \phi$. Where ϕ is the phase angle between stress and strain. The source of the inconsistency is shown to be the definition of maximum strain energy, which may be straightforwardly misapplied to the entire area under a hysteresis loop when the experiment is entirely in compression. This results in the Q^{-1} that is four times less than the phase angle Q^{-1} . In order to resolve the conflict, the origin of zero stress and strain must always be located at the center of the hysteresis loop before the definition $Q^{-1} = \delta W / 2\pi W$ is applied. Accordingly, the resulting Q^{-1} must be associated with the material condition at the center of the loop.

The second paper in this report is an investigation of the frequency dependence of attenuation and moduli for Sierra White granite utilizing three laboratory techniques: hysteresis loop, resonant bar, and ultrasonic pulse. The hysteresis loop and resonant bar results for room dry granite indicate that Young's modulus and extensional attenuations ($Q_e^{-1} \sim 0.008$ to 0.006) are nearly constant over a broad frequency range including 0.1 Hz and from 10 kHz to at least 200 kHz. The attenuation mechanism for room dry samples is closely related to adsorbed moisture on the surfaces of cracks. For the water saturated samples, hysteresis loop and resonant bar extensional attenuations increased dramatically, by factors of four to seven and one-half. The corresponding Young's modulus was either unchanged for the fundamental resonant bar frequency or decreased slightly for the hysteresis loop experiment. In addition, resonant bar attenuations in the range 10-90 kHz decreased with increasing frequency, consistent with a relaxation peak in the extensional attenuation spectra at a frequency below 10 kHz. The

attenuation mechanism at these frequencies is local viscous flow of pore fluid in microcracks and between adjacent pore spaces.

Ultrasonic results in three frequency bands between 40 kHz and 1.1 MHz show that although the dry Young's modulus agrees with the resonant bar and hysteresis loop data, attenuation is larger and increases rapidly with frequency. When the frequencies of the ultrasonic and resonant bar techniques overlap, ultrasonic attenuation is larger by a factor of 3 to 4. A dominant attenuation mechanism at ultrasonic frequencies is probably scattering. The scattering attenuation mechanism is also combined with fluid losses, however, since Q_e^{-1} and Q_s^{-1} increase in the saturated sample at 0.6 - 1.1 MHz. On the other hand, Q_p^{-1} actually goes down upon saturation, an observation that correlates well with scattering since the cross-sectional area of the scatterers is reduced by the presence of pore fluid. Confining pressure closes or reduces the size of microcracks, increasing velocities and reducing attenuation. At high pressures the dry and saturated velocities and attenuations converge.

The Definition and Calculation of Q^{-1} in Hysteresis Loop Attenuation Measurements

Karl B. Coyner
New England Research, Inc.
76 Olcott Drive
White River Junction, VT 05001

Abstract. An inconsistency in the interpretation of experimental stress-strain data for attenuation determinations is investigated. Attenuation (Q^{-1}) calculated from the integrated areas of plotted hysteresis loops depend on the definition of maximum strain energy. If maximum strain energy is taken as the entire area under the loading segment of the hysteresis loop, the resulting Q^{-1} are approximately 4 times less than the Q^{-1} from the phase angle ϕ measured between cycled stress and strain ($Q^{-1} = \tan \phi$). This inconsistency is resolved by locating the origin of zero stress and strain at the center of the hysteresis loop, regardless of the absolute sign of stresses and strains, and calculating the maximum strain energy during one cycle relative to that origin. Attenuation calculated from the ratio of hysteresis loop areas must be carefully interpreted before application to seismic wave propagation.

Introduction

From a seismological perspective the hysteresis loop technique probably provides the most relevant and acceptable laboratory determinations of rock attenuation and moduli. This is because seismic frequencies between approximately 0.01 and 400 Hz and strain amplitudes between 10^{-7} and 10^{-3} have been attained (Gordon and Davis, 1968; Walsh et al., 1970; Mckavanaugh and Stacy, 1974; Liu and Peselnick, 1983; Jackson et al., 1984; Stoll, 1985; Coyner, 1990). The technique involves direct measurements of the stress-strain response of rock during an applied periodic stress. This stress may be uniaxial compressional loading, torsional shear, or bulk hydrostatic compression. This method provides critical experimental data that can be used to formulate constitutive properties of rock. This data can be used in models of high strain, nonlinear attenuation (Minster and Day, 1986), and allows interpretations of fundamental attenuation mechanisms (Spencer, 1981). At present there is only a limited set of laboratory data available. Much of it is contradictory and perhaps improperly presented as Q^{-1} data because of an inconsistency in the definition of maximum strain energy as applied to hysteresis loop analysis.

In the hysteresis loop technique, attenuation may be calculated from either the phase angle ϕ between cycled stress and strain (Spencer, 1981; Jackson et al., 1984) or from the hysteresis loops generated by plotting the stress versus strain data (Gordon and Davis, 1968; Walsh et al., 1970; McKavanagh and Stacey, 1974; Brennan, 1981; Liu and Peselnick, 1983). In the former, the phase angle is determined by signal analysis of stress-strain cycles obtained with the aid of computer-based data collection and analysis algorithms. The attenuation is given by the relation $Q^{-1} = \tan \phi$. In the latter, the hysteresis loops are plotted. The attenuation is defined as $Q^{-1} = \delta W / 2\pi W$, where δW is the dissipated strain energy and W is the maximum strain energy introduced into the sample during one stress-strain cycle. The area of the hysteresis loop is proportional to δW and the area under the increasing load portion of the loop is proportional to W . Q^{-1} is calculated by integrating these respective areas of the hysteresis loop. Note that absolute areas, or strain energies, are not important since a ratio is calculated.

Although these two data reduction techniques appear straightforward, a thorough comparison has apparently not been made in previous experimental investigations. Presumably, they should duplicate each other because of the equivalency $Q^{-1} = \tan \phi = \delta W / 2\pi W$. A closer examination of the techniques and published results, however, has revealed a caveat in the analysis of the plotted hysteresis loops. The potential result is an incorrect Q^{-1} that is four times less than the true value or that indicated by the tangent of the phase angle.

The source of this potential error is the definition of maximum strain energy and the relative location of the origin for zero stress and strain. The accepted definition, from which the equivalency is derived, is appropriate for sinusoidal signals centered about zero stress and strain, i.e., a rock undergoing both compression and tension, for which the origin is at the center of the hysteresis loop. In this case the maximum strain energy calculated for the compressive portion of the loop is approximately 1/4th of the overall peak to peak energy function.

If, on the other hand, the hysteresis loop is displaced on the stress-strain plot, the maximum strain energy changes. This is exactly what happens in many laboratory measurements, which are normally biased by a pre-stress or simply run over a sequence of continuously positive stresses and strains. For these measurements the maximum strain energy stored in a cycle is the whole area under the hysteresis loop, which is, equivalently, taking the origin at the point of lowest stress and strain. The maximum strain energy is approximately a factor of 4 greater than the above definition. This results in a lower Q^{-1} by a factor of 4. An accounting of this factor of 4 is significant in comparing various experimental results that have utilized either of the two techniques.

Hysteresis Loop Analysis

The time-varying stress $\sigma(t)$ and strain $\epsilon(t)$ functions that describe a linear anelastic material deformed by a steady-state sinusoidal stress of frequency ω and amplitude σ_0 are derived to be as follows

$$\sigma(t) = \sigma_0 \sin(\omega t)$$

$$\epsilon(t) = J \sigma_0 \sin(\omega t - \phi).$$

Where J is a compliance. Since the material is anelastic the strain lags stress in time by the phase angle, ϕ . The strain function may be expanded,

$$\epsilon(t) = J_1 \sigma_0 \sin(\omega t) - J_2 \sigma_0 \cos(\omega t)$$

to yield "in phase", $\sin(\omega t)$, and "out-of-phase" $\cos(\omega t)$ strain components, where $J_1 = J \cos\phi$ and $J_2 = J \sin\phi$. The ratio of the magnitudes, or the real and imaginary parts of the strain function, is $\tan \phi = J_2 / J_1$.

The hysteresis loop is a plot of the stress-strain relationship described by these functions and is an ellipse with the origin centered at zero stress and strain. A hysteresis loop that was generated by introducing a phase angle of 0.0628 radians between two sine waves is shown in Figure 1. The maximum and minimum stresses and strains are $\pm \sigma_0$ and $\pm J \sigma_0$, respectively, and the hysteresis loop is traced out in a clockwise direction.

The phase angle and the hysteresis loop are both equivalent expressions of the same anelastic process through which energy is absorbed. A dimensionless measure of anelasticity is the Q factor, which is an analogue of the Q used for characterizing the efficiency of voltage transfer in electric circuits. The inverse of Q may be called the dissipation factor (Q^{-1}), two expressions for which are

$$Q^{-1} = \tan \phi$$

and

$$Q^{-1} = \delta W / 2\pi W$$

The first expression is the "loss tangent" and refers to the tangent of the phase angle between stress and strain. In the second expression relative attenuation is obtained from the ratio of δW , the energy dissipated during one cycle, to the maximum strain energy W

introduced into the sample during one cycle.

The two definitions are equal for the linear anelastic material described by the sinusoidal stress and strain time functions given above. This is easily shown by considering the hysteresis loop in Figure 1. If stress times strain is defined as strain energy, then the areas within the hysteresis loop plot contain all of the necessary information for calculating the relative attenuation energy ratio. The maximum energy W supplied to the material is the shaded area of Figure 1, corresponding to the deformation between points A and B, or the integral

$$W = \int_A^B \sigma d\epsilon$$

The dissipated energy δW is the cross-hatched area contained within the hysteresis loop and is defined in the integral form

$$\delta W = \int_c^B \sigma_{\text{upper}} d\epsilon + \int_B^c \sigma_{\text{lower}} d\epsilon$$

The integrals can be easily solved by noting from Figure 1 that W is approximately the area of a triangle with sides σ_0 and $J \sigma_0$, and δW is the area of an ellipse with semi-major axis along the slope $1/J$ and semi-minor axis along the slope $-1/J$. The lengths of the axes can be calculated from the intersections with the equation for the ellipse obtained from the stress-strain relation. The two integrals can therefore be geometrically computed for small attenuations as

$$W \approx J_1 \sigma_0^2 / 2$$

and

$$\delta W \approx \pi \tan \phi J_1 \sigma_0^2$$

Substituting for the ratio $W/\delta W$, it is found that

$$Q^{-1} = \delta W / 2\pi W = \tan\phi$$

and the definitions are thereby equivalent. For the hysteresis loop in Figure 1, $Q^{-1} = 0.0629$ ($Q = 15.9$).

For nonlinear materials and large attenuations the hysteresis loop becomes nonelliptical and nonsymmetrical, with cusped ends (McKavanagh and Stacey, 1974). In this instance it is necessary to integrate the areas of the hysteresis loop directly and to calculate Q^{-1} from the energy ratio. The phase angle between stress and strain is not singularly defined in this case as the strain sinusoid is distorted.

Although the analysis of hysteresis loops is well-known (see, for example, Lorrain and Corson, 1970), an essential point is that the stress and strain functions are AC-signals, that is, centered about zero with equal positive and negative excursions and a hysteresis loop centered on the origin. Consequently, the maximum strain energy $\approx J \sigma_0^2 / 2$ is attained in only one-half of the overall peak-to-peak stress and strain amplitudes ($2\sigma_0$ and $2J \sigma_0$, respectively).

If the sinusoidal stress and strain time functions are DC-biased, i.e., offset so that they are continuously positive, the definitions of maximum strain energy W , energy dissipation δW , and the identity of the hysteresis loop origin can become somewhat confusing. In Figure 2, the same hysteresis loop as in Figure 1 is replotted with the origin at zero stress and strain. The stress and strain time functions for this hysteresis loop have been shifted by $+\sigma$ and $+J \sigma_0$, although with the same peak-to-peak amplitudes of $2\sigma_0$ and $2J \sigma_0$. The energy dissipated during a cycle is still the area of the ellipse, as in Figure 1, or $\pi \tan\phi J_1 \sigma_0^2$. Maximum strain energy, however, or the shaded area under the loading portion of the hysteresis loop in Figure 2, is

$$W = (2 \sigma_0) (2 J_1 \sigma_0) / 2 = 2 J_1 \sigma_0^2$$

a factor of 4 times greater than before. Accordingly, when δW and W are substituted into the relative attenuation definition, the result is

$$Q^{-1} = \delta W / 2\pi W = (\tan\phi) / 4$$

Since the DC-bias has not changed the phase angle between stress and strain, the "loss-tangent" definition of attenuation remains $Q^{-1} = \tan\phi$. The immediate and perplexing result is that the attenuation factor calculated from the hysteresis loop areas is 1/4th of that

calculated from the tangent of the phase angle.

This apparent inconsistency can be resolved by examining the maximum strain energy W relative to the origin of the hysteresis loop in Figure 2. From the external perspective, the sinusoidal stress deforming the material generates maximum strain energy that is indeed $2J_1 \sigma_0^2$. For the material, however, the state of stress and strain appropriate for the hysteresis loop and energy calculation is not at the origin of zero stress and strain in Figure 2, but at the center of the hysteresis loop, i.e., as in Figure 1. Although stress and strain are continuously positive, the material at $+\sigma_0$ stress and $+J \sigma_0$ strain is being cyclically deformed by stress and strain functions with amplitudes of $\pm \sigma_0$ and $\pm J \sigma_0$. Once this reference at the center of the hysteresis loop in Figure 2 is adopted, the maximum strain energy is reduced to what it was for the hysteresis loop in Figure 1, $J_1 \sigma_0^2 / 2$. The attenuation from the relative energy attenuation ratio and loss tangent then agree, $Q^{-1} = \delta W / 2\pi W = \tan \phi$.

An important point is that the attenuation must be associated with the deformed condition of the material at the center of the hysteresis loop. Therefore, true attenuation at zero stress and strain requires both tension and compression (or both signs of shear) in the hysteresis loop. If, on the other hand, the hysteresis loop starts at zero stress and strain, as in Fig. 2, the measured attenuation is associated with the material at $+\sigma_0$ and $+J \sigma_0$.

Discussion

Although the clarification of hysteresis loop analysis for attenuation is straightforward, the inconsistency has propagated through much of the available experimental stress-strain data. Therefore, previous results are re-evaluated with respect to this factor of 4. This resolves at least one outstanding discrepancy and increases (by a factor of 4) several sources of Q^{-1} data for rock. This is particularly important if attenuations are to be interpreted and compared with other results (field observations, resonant bar, ultrasonic).

There are two techniques to measure and interpret attenuation from low-frequency stress-strain data. Either the phase angle is measured directly (Spencer, 1981; Jackson et al., 1984) or else the hysteresis loop is plotted out and the areas integrated (Gordon and Davis, 1968; Walsh et al., 1970; McKavanagh and Stacey, 1974; Brennan, 1981; Liu and Peselnick, 1983; Coyner, 1987). Hysteresis loop integration of the areas shown in Figure 2 and discussed in the analysis section leads to a Q^{-1} that is less than the loss tangent $Q^{-1} (\tan \phi)$ by a factor of 4. Therefore, in most instances the Q^{-1} obtained by analyzing the areas of hysteresis loops have to be increased by a factor of 4. This is particularly true if they are to be interpreted and compared with the Q^{-1} results of other experimental techniques (field observations, resonant bar, ultrasonic.)

Table 1 is a tabulation of experimental Q^{-1} from previous low frequency, stress-strain experiments on nominally dry and vacuum dry rocks that were measured with either the phase angle or plotted hysteresis loop technique. The rock type, frequency, strain amplitude, and "reported" Q^{-1} are collected from the various references given in Table 1. The "corrected" values have been calculated using the analysis outlined above, i.e., reported Q^{-1} 's multiplied by a factor of 4. Spencer (1981) and Jackson et al. (1984) measured the phase angle directly and, consequently, their results do not require correction (References 5 and 7). For all of the others (Table 1) either the plotted hysteresis loops or a statement of procedure indicates that maximum strain energy was integrated under the entire loop, resulting in an underestimated Q^{-1} by a factor of 4. One exception is Walsh et al. (1970), who report their attenuation results as relative attenuation, $\delta W / W$, and not as Q^{-1} . Nevertheless, in order to interpret the results as Q^{-1} the relative attenuations still need to be divided by 8π .

The strain amplitude dependence of attenuation changes quite dramatically if large strain amplitude Q^{-1} are increased by a factor of 4. Gordon and Davis (1968) found that hysteresis loop attenuation data at large strain amplitudes ($>10^{-4}$) was essentially equal to resonant bar attenuations at low strain amplitudes ($<10^{-6}$), even though resonant bar data indicated a rapid increase in attenuation at intermediate strain amplitudes. The correction increases hysteresis loop attenuations by a factor of 4. This results in a monotonically increasing attenuation with strain amplitude, independent of experimental technique.

This is a far more plausible result because it is consistent with models of the frictional attenuation mechanism (Walsh, 1966; Mavko, 1979; Stewart et al., 1983). At low strain amplitudes, less than 10^{-6} strain, attenuation is linear or independent of strain amplitude. Q^{-1} 's are quite low (Table 1, references 5, 6, and 7). Above that point attenuation increases rapidly as nonlinear friction becomes dominant along crack and pore surfaces. Q^{-1} may become extremely large at strain amplitudes above 10^{-4} , on the order of 10 to several hundred ($1000/Q$, Table 1, references 1, 2, and 3). In this group the Q^{-1} for microcracked granites fall in the range from 15 to 90 ($1000/Q$, references 1, 2, 3, and 4). The Q^{-1} of several hundred is for a friable, weathered, Cedar City diorite (Walsh et al., 1970).

A discrepancy that is resolved when hysteresis loop Q^{-1} are increased by a factor of 4 is the unexpected similarity of Q^{-1} data of Liu and Peselnick (1983) compared to that of Spencer (1981). Both conducted hysteresis loop experiments on cylinders of granite at low frequencies and low strain amplitudes. Liu and Peselnick, however, found a small Q^{-1} (<2.0) for room dry Westerly granite. This is a saturation condition that contrasts with the large Q^{-1} (>500) observed by Spencer for vacuum dry Oklahoma granite. These similar results seem unusual since the work of Tittmann (1977) and Clark et al. (1980) has underscored the substantial increase in Q^{-1} caused by the presence of volatiles, particularly water. Resonant bar measurements by Coyner (1987) on room dry Sierra White granite

found Q^{-1} to be approximately 0.125, similar to that found by Winkler et al. (1979) for Sierra White and Tittmann (1984) for Westerly granite. Therefore, the Liu and Peselnick data point appears anomalous because the Q^{-1} is so small for a room-dry rock at zero confining pressure. If the hysteresis loop data of Liu and Peselnick are re-interpreted, and the Q^{-1} increased by a factor of 4, to $Q^{-1} < 0.0089$, small Q^{-1} 's or typical microcracked granite are therefore preserved for vacuum conditions (Spencer, 1981) or samples under confining pressure (Jackson et al., 1984).

The hysteresis loop analysis indicates the attenuation factors determined for a particular hysteresis loop have to be associated with the stress-strain status of the material at the center of the hysteresis loop. This has several implications for experimental procedure. First, in order to characterize the strain amplitude dependence of a rock material the center of all hysteresis loops must coincide. This would presumably be at the center of the largest amplitude hysteresis loop, so this implies a large initial state of stress. Secondly, in order to measure large strain amplitudes at zero or near-zero stress a negative stress or tension would be required. A preliminary investigation of attenuation in tension has been made by Bulau and Tittmann (1985).

Although modern experimental technique and digital signal processing favors the direct measurement of phase angle in hysteresis loop experiments, the analysis of hysteresis loop areas is still important for problems in nonlinear anelasticity. At large strain amplitudes friction distorts the strain signal and hysteresis loops undergo a transition from elliptical to cusped shapes (Brennan and Stacey, 1977). The phase angle is no longer unique and hysteresis loops must be integrated in order to obtain accurate attenuations. In addition, the shape of cusped loops may reveal the dynamics of frictional processes.

Conclusion

It has been shown that direct stress-strain calculations of attenuation can lead to inconsistent results when comparing phase angle with hysteresis loop measurements. Q^{-1} 's derived from the areas of hysteresis loops must be multiplied by a factor of 4 in order to be comparable to those from the phase angle, if the maximum strain energy is taken as the entire area under the loading portion of the hysteresis loop. Previous experimental data must be interpreted and compared in light of this correction factor. In particular, the strain amplitude dependence of attenuation is greater than previously realized, and room dry granite can have Q^{-1} 's as large as several hundred at amplitudes greater than 10 microstrain.

REFERENCES

- Brennan, B.J., and F.D. Stacey, Frequency dependence of elasticity of rock-test of seismic velocity dispersion, *Nature*, 268, 220-222, 1977.
- Brennan, B.J., Linear viscoelastic behavior in rocks, in *Anelasticity in the Earth, Geodyn. Ser.*, vol.4, edited by F.D. Stacey, M.S. Paterson, and A. Nicolas, pp. 13-22, AGU, Washington, D.C., 1981.
- Bulau, J.R., and B.R. Tittman, Nonlinear wave propagation study, final report to Air Force Office of Scientific Research, Contract No. F49620-83-C-0065, 1985.
- Clark, V.A., B.R. Tittman, and T.W. Spencer, Effects of volatiles on attenuation (Q^{-1}) and velocity in sedimentary rocks, *J. Geophys. Res.*, 85, 5190-5198, 1980.
- Coyner, K.B., Attenuation measurements on dry Sierra White granite, dome salt, and Berea sandstone, final report to Lawrence Livermore National Laboratory, Contract #9092405, 1987.
- Coyner, K.B., Comparison of hysteresis loop, resonant bar, and ultrasonic attenuation measurements on Sierra White granite, manuscript in preparation, 1990.
- Gordon, R.B., and L.A. Davis, Velocity and attenuation of seismic waves in imperfectly elastic rock, *J. Geophys. Res.*, 73, 3917-3935, 1968.
- Jackson, I., M.S. Paterson, H. Niesler, and R.M. Waterford, Rock anelasticity measurements at high pressure, low strain amplitude and seismic frequency, *Geophysical Research Letters*, 11, 1235-1238, 1984.
- Liu, H.-P., and L. Peselnick, Investigation of internal friction in fused quartz, steel, plexiglass, and Westerly granite from 0.01 to 1.00 Hertz at 10^{-8} to 10^{-7} strain amplitude, *J. Geophys. Res.*, 88, 2367-2379, 1983.
- Lorrain, P., and D. Corson, *Electromagnetic Fields and Waves*, 2nd edition, W.H. Freeman and Company, San Francisco, p. 396-400.
- Mavko, G.M., Frictional attenuation: An inherent amplitude dependence, *J. Geophys. Res.*, 84, 4769-4775, 1979.

McKavanagh, B., and F.D. Stacey, Mechanical hysteresis in rocks at low strain amplitudes and seismic frequencies, *Physics of the Earth and Planetary Interiors*, 8, 46-250, 1974.

Minster, J.B., and S.M. Day, Decay of wave fields near an explosive source due to high-strain, nonlinear attenuation, *Journal of Geophysical Research* 91, 2113-2122, 1986.

Spencer, J.W., Stress relaxations at low frequencies in fluid-saturated rocks: Attenuation and modulus dispersion, *J. Geophys. Res.*, 88, 546-554, 1983.

Stewart, R.R., M.N. Toksoz, and a. Timur, Strain amplitude attenuation: Observations and a porposed mechanism, *J. Geophys. Res.*, 88, 546-554, 1983.

Stoll, R.D., Marine sediment acoustics, *J. Acoust. Soc. Am.*, 77, 1789-1799, 1985.

Tittmann, B.R., Internal friction measurements and their implications in seismic Q structure models of the crust, in *The Earth's Crust: Monograph 20*, AGU, 197-213, 1977.

Tittmann, B.R., Nonlinear wave propagation study, semi-annual technical report No. 2 for the period December 1, 1983 through May 31, 1984, SC5361.6SAR, Rockwell International Science Center, 1984.

Walsh, J.B. Seismic wave attenuation in rock due to friction, *J. Geophys., Res.*, 71, 2591-2599, 1966.

Walsh, J.B., W.F. Brace, and W.R. Wawersik, Attenuation of stress waves in Cedar City quartz diorite, Technical Report No. AFWL-TR-70-8, M.I.T., 1970.

Winkler, K.W., A. Nur, and M. Gladwin, Friction and seismic attenuation in rocks, *Nature*, 277, 528-531, 1979.

TABLE 1. Reported and Corrected Hysteresis Loop Q^{-1} Factors.

Rock (Dry)	Frequency (Hz)	Strain (10^{-6})	Mode	1000* Q^{-1}		Reference
				Reported	Corrected	
Granite	.0005-.05	10^2 - 10^3	Ext	15	60	1
Quartzite	.0005-.05	10^2 - 10^3	Ext	5	20	1
Granite (Cedar City)	<.05	10^3 - 10^4	Ext	125-91*	500-360	2
Granite (Westerly)	<.05	500	Ext	22*	88	2
Granite, basalt, and sandstone	.003-.1	1-10	Ext	10	40	3
Basalt	.001-.5	1.7	S	1.90	7.62	4
Granite	.001-.5	1.1	S	3.76	15.0	4
Sandstone	.001-.5	1.2	S	13.3-8.0	52.6-32.3	4
Sandstone, granite, limestone (vacuum dry)	.004-.4	0.1	Ext	<2.0	<2.0	5
Granite (Westerly)	.01-1	.01-.1	Ext	<2.0	<8.9	6
Granite ($P_c > 10$ MPa)	.33-.003	0.6	S	2.5-0.5	2.5-0.50	7

References: 1, Gordon and Davis, 1968; 2, Walsh et al., 1970; 3, McKavanagh and Stacey, 1974; 4, Brennan, 1981; 5, Spencer, 1981; 6, Liu and Peselnick, 1983; 7, Jackson et al., 1984.

*converted from reported relative attenuations.

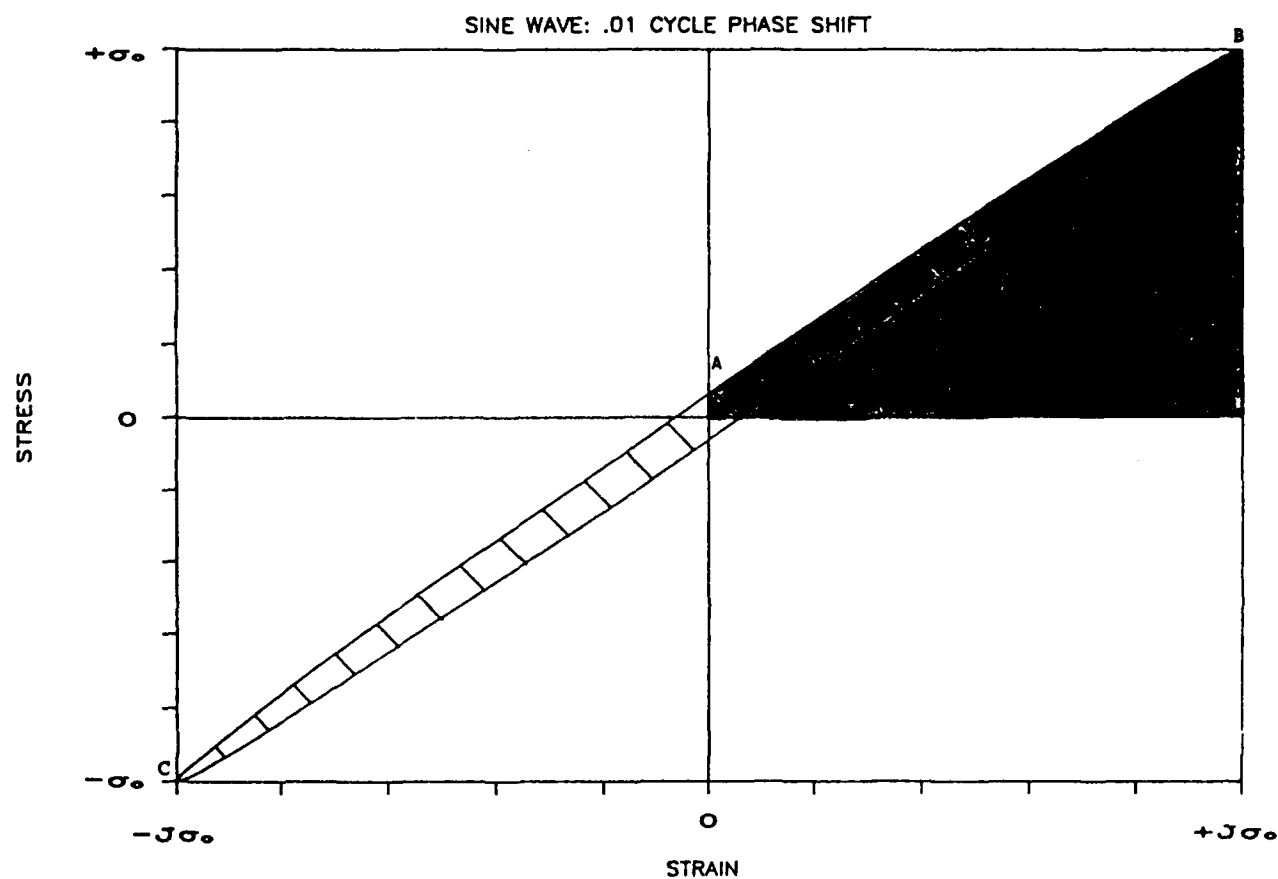


Figure 1. Hysteresis loop derived from two sine waves offset by 0.01 cycles, or 0.0628 radians, centered at zero stress and strain. The shaded area is the maximum energy W introduced into a unit volume of sample during one cycle, corresponding to the path from A to B on the hysteresis loop. The interior area of the hysteresis loop δW is the energy dissipated per unit volume during one cycle. The attenuation is $Q^{-1} = \delta W / 2\pi W = \tan\phi = (.0628)$.

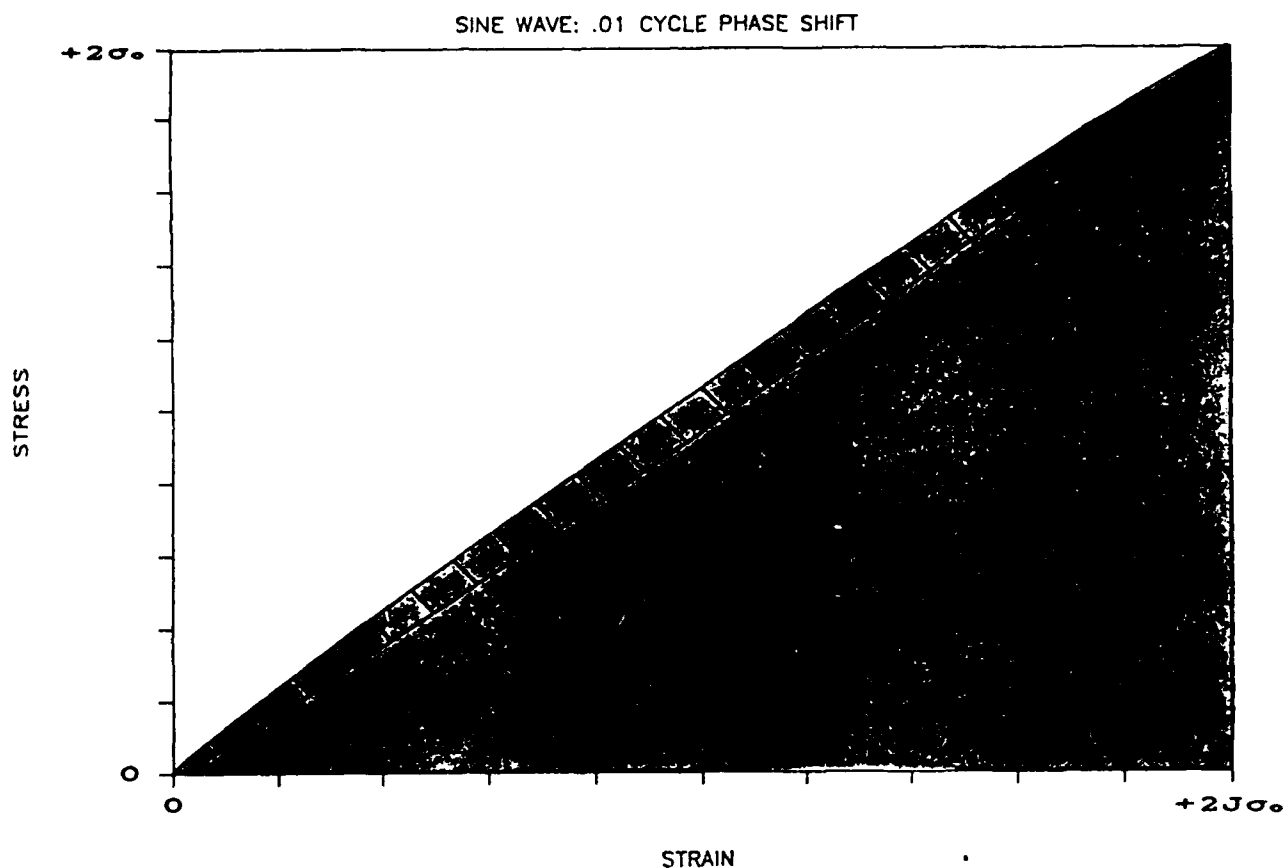


Figure 2. Same hysteresis loop as in Figure 1, but centered at $+\sigma_0$ stress and $+J\sigma_0$ strain. The shaded area is the maximum energy introduced per unit volume during the hysteresis loop cycle, but this gives an incorrect relative attenuation ($1/4Q^{-1}$) for the material at stress $+\sigma_0$ and $+J\sigma_0$ strain, for which this hysteresis loop is representative.

Comparison of Hysteresis Loop, Resonant Bar, and
Ultrasonic Attenuation Measurements on Sierra White Granite

Karl B. Coyner
New England Research, Inc.
76 Olcott Drive
White River Junction, VT 05001

Abstract. Attenuation and dynamic moduli measurements on intact Sierra White granite samples were performed utilizing three experimental techniques: hysteresis loop, resonant bar, and ultrasonic spectral ratio. Extensional attenuations (Q_e^{-1}) and Young's moduli were measured at 0.1 Hz with the hysteresis loop and between 10 and 210 kHz with the resonant bar techniques. Ultrasonic P and S wave velocities and spectral ratio compressional (Q_p^{-1}) and shear (Q_s^{-1}) attenuations were measured in the 100-200 kHz and 0.6 - 1.1 MHz frequency bands, then converted into comparable extensional attenuations and Young's moduli. Compressional velocities and attenuations were also measured at 40-80 kHz. Both room dry and water saturated samples were investigated with all three techniques, and ultrasonic measurements at 0.6 - 1.1 MHz were conducted as a function of confining pressure to 100 MPa.

The Young's moduli for room dry samples are approximately the same (~34 to 35 MPa) at all frequencies, and the hysteresis loop and resonant bar Q_e^{-1} 's are small and comparable to within experimental error (~0.008 to 0.006). The attenuation mechanism is related to small amounts of water adsorbed onto the surfaces of microcracks. In contrast, ultrasonic Q^{-1} 's for room dry samples are much larger and increase quite rapidly with increasing frequency between the three different ultrasonic frequency bands. Between 100 and 200 kHz spectral ratio attenuations ($Q_e^{-1} = 0.024$) are approximately 3 times larger than resonant bar attenuations ($Q_e^{-1} = 0.0053$). A scattering attenuation mechanism for ultrasonic pulses is suggested by these observations.

Water saturation dramatically increases the hysteresis loop and resonant bar Q_e^{-1} 's by factors of 3 and 7.5, respectively, but has a minimal effect on Young's modulus. In contrast, the 0.6 - 1.1 MHz ultrasonic data reveal that Young's modulus nearly doubles while Q_e^{-1} only increases from 0.058 to 0.075. The 0.6 - 1.1 MHz compressional attenuation Q_p^{-1} actually decreases upon saturation, from 0.065 to 0.046, while the 40-80 kHz Q_p^{-1} increases from 0.020 to 0.064. The reduction of attenuation at the higher frequencies provides additional evidence of scattering; scattering cross-sections are reduced when fluid is introduced. The large increase in saturated modulus reflects the unrelaxed dynamic response of pore fluid at ultrasonic frequencies. Attenuation is enhanced at lower frequencies by a dynamic viscous fluid flow mechanism. A relaxation peak in the attenuation spectrum below approximately 10 kHz is indicated by decreasing resonant bar Q_e^{-1} 's as a function of increasing frequency to 90 kHz.

Introduction

Laboratory determinations of dynamic attenuation and moduli in rock reply on three principal experimental techniques: ultrasonic, resonant bar, and hysteresis loop. They differ substantially in both experimental arrangement and frequency bandwidth. Ultrasonic experiments are typically performed at frequencies around 1 MHz, with P and S-wave attenuations determined by spectral ratio analysis of broadband pulses propagated through both the rock and a low loss standard (Toksoz et al., 1979). At intermediate frequencies, between 500 Hz and 100 kHz, the resonant bar technique is utilized to measure attenuation from the decay or spectral width of extensional, flexural, and torsional resonances in cylindrical rods of material (Tittmann, 1977, Winkler, 1979). At lower frequencies, the hysteresis loop technique measures attenuation and modulus on samples subjected to cyclical stress-strain paths at frequencies between 0.01 and 500 Hz (Spencer, 1981; Peselnick and Outerbridge, 1961; Gordon and Davis, 1968; Liu and Peselnick, 1983).

In this study attenuation and moduli data collected on Sierra White granite with the three experimental techniques are compared. Sierra White granite is a fine-grained, muscovite-biotite granite with a bulk density of 2.638 g/cc, porosity of 0.8%, and a mean grain diameter of 0.70 mm. The modal analysis composition is 44% microcline, 32% quartz, 6% albite, 11% biotite, and 5% muscovite. The samples were obtained from a single block at the Raymond Quarry in Raymond, California. Macroscopic inspection of samples plus deformation and ultrasonic P and S-wave velocity measurements revealed homogeneous characteristics with elastic anisotropy of less than 5%. Experiments were conducted on several samples cored or cut from the same original quarry block.

EXPERIMENTAL TECHNIQUES AND PROCEDURES

Hysteresis Loop Experiments

The hysteresis loop technique was used to investigate extensional attenuation and dynamic Young's modulus at low frequency in dry and saturated Sierra White granite. In this technique, the strain response of a sample subjected to a continuous sinusoidal stress is measured. The technique was similar to that employed by Spencer (1981) and Liu and Peselnick (1983). The phase difference between strain and the driving stress is one definition of attenuation, and may be measured directly with Fourier phase analysis.

Hysteresis loop measurements were performed on a precisely ground cylinder of Sierra White granite that was 0.15 meters in diameter and 0.51 meters long. The sample was

instrumented with three axial LVDT displacement transducers mounted on two circumferential rings positioned with radial screws near each end of the sample (Fig. 1). The LVDT barrels were axially mounted in one ring, while the LVDT cores were attached to the second ring with extension rods. This sample assembly was located in series with a precision load cell in a servo-controlled loading frame. The sample was exposed to the atmosphere at room temperature and the sample column was pre-loaded to a constant axial stress of 0.1 MPa. A sinusoidal, 0.1 Hz, axial stress was then applied to one end of the sample with a servo-controlled ram operating in force feedback mode. A PC-based D/A converter was used to generate the 0.1 Hz controlling signal. A voltage divider on the D/A output controlled the amplitude of the force, thereby also controlling the strain amplitude. Axial force from the load cell and sample displacement from the LVDT transducers were measured and recorded with a PC-based A/D converter as a function of load and strain amplitude. The data were recorded over many cycles in order to average noise. The sample was measured both dry and water-saturated while exposed to the atmosphere at room temperature. A sheet of plastic film was used to cover the water-saturated sample in order to prevent drying.

The axial load and displacement data were converted to axial stress and strain data by simple division with sample cross-sectional area and the ring separation distance, respectively. The three individual LVDT signals were averaged. Extensional attenuations were calculated from the tangent of the phase angle ϕ between stress and strain determined by FFT analysis ($Q_e^{-1} = \tan \phi$). Young's moduli were calculated from the least-squares fit of a straight line through the hysteresis loop. Up to several hundred stress cycles were collected in order to obtain repeatable phase angles. Low strain amplitude ($\sim 10^{-6}$) linear anelastic data were used to compare with the low strain amplitude data collected with the other techniques.

The errors in the load and strain measurements were on the order of 1% or less. The phase angle calculation incurred a relatively larger error based on the ability to obtain repeatable phase angles, and the corresponding Q^{-1} factors are precise to $\pm 15\%$.

Resonant Bar Experiments

Benchtop resonant bar experiments were conducted on a slender square rod of Sierra White granite 0.00635 meters square on a side and 0.171 meters in length. The sample was measured unjacketed in the room dry and water-saturated condition while exposed to the atmosphere at room temperature. The sample was driven in extensional resonance modes with high frequency (1.0 MHz) compressional piezoelectric ceramic crystals epoxied to both sample ends (Fig. 2). One crystal was arbitrarily identified as the excitation source and the second as the receiver. The sample was supported in free air on

the bench with a fixture that supported the sample at its midpoint. A lock-in amplifier was used to resonate the rod at the fundamental extensional resonance (approximately 10.3 kHz) and at higher harmonics, up to the 20th harmonic for the dry sample and up to the 8th harmonic for the saturated sample. Both source and sensing piezoelectric crystals were wired to the amplifier, one to the reference sine wave output and the second to the differential amplifier input. The differential amplifier input from the sensing crystal was able to "lock-in" to the phase-shifted sine wave frequency being used to resonate the rod. A PC-controlled D/A converter was used to externally control the lock-in amplifier reference sine wave output to sweep through the entire frequency band of interest, and an A/D input was used to measure the amplified signal from the sensing crystal.

Extensional attenuation was calculated by dividing the halfpower width (Δf) of the resonant peak by the center frequency f : $Q_e^{-1} = \Delta f/f$. Extensional velocity was calculated by dividing the wavelength of the mode by the center frequency. Young's modulus was calculated from the square of extensional velocity times the density. An error of less than 5% can be associated with the attenuation and modulus from this resonant bar experiment.

Ultrasonic Experiments

Ultrasonic velocity and attenuation measurements were performed on three different Sierra White granite samples with three different frequency bandwidth ultrasonic transducers. The three samples included the 0.51 m long cylinder used in the hysteresis loop experiments, a smaller cylinder 0.076 m in diameter by 0.152 m long, and a cubic block 0.203 m long on each side. One set of ultrasonic transducers was capable of propagating either P or S waves in the 100-200 kHz frequency band, and a second set in the 0.6-1.1 MHz frequency band. A set of P wave transducers operated at 40-80 kHz. The low frequency transducers (100-200 kHz and 40-80 kHz) were designed for benchtop velocity and attenuation measurements at very low loads while the high frequency transducers (0.6-1.1 MHz) were designed for either benchtop or high confining and pore fluid pressure (to 200 MPa) measurements.

Various ultrasonic velocity and attenuation measurements were made on the Sierra White granite samples with the different ultrasonic transducers. Measurements on the large 0.51 m cylinder were conducted in order to compare with the hysteresis loop results. A sample of this size was necessary for the 40-80 kHz transducers, and benchtop measurements were made on both the dry and saturated sample. The smaller 0.15 m long cylinder was measured dry and saturated with the 0.6 - 1.1 MHz P and S-wave transducers

in both a benchtop configuration and as a function of confining pressure to 100 MPa. Finally, the 0.203 m block was measured in the dry saturation with the 100-200 kHz transducers. Measurements were also carried out on aluminum standards for the spectral ratio analysis.

The experimental apparatus included the specially constructed ultrasonic transducers, a pressure vessel system capable of applying hydrostatic confining pressure and pore fluid pressure, and electronic equipment (Fig. 3). Ultrasonic transducers were developed and constructed to produce reproducible signals at the various frequencies. The higher frequency transducers incorporated both P and S crystals so that either signal could be propagated during an experiment. At 50 kHz a satisfactory S-wave signal could not be produced and only a P-wave crystal was used.

The electronic equipment used in the experiments include switches, a pulse generator, amplifier, filter, and digital oscilloscope, and a computer (Fig. 3). a source and receiver pair of like crystals (P or S) were selected, and the source crystal was excited by a fast risetime electrical pulse generated with a Panametrics 5055PR pulser-receiver or a higher power pulse. The crystal produced a broadband ultrasonic pulse that propagated through the adjacent metal plate to which the crystal was epoxied, through the rock sample along the core axis, through the metal plate of the receiving transducer, and into the receiver crystal. The electrical signal produced by the receiver transducer was amplified and filtered by the receiving section of the Panametrics 5055PR, then digitized by a LeCroy 9400 digital oscilloscope. The signals were typically amplified by 20 to 40 dB and high-pass filtered. The oscilloscope displayed the signal for the travel time pick and the digitized signal was transferred to the computer for subsequent spectral attenuation analysis. With this system it was possible to acquire well-defined, broadband P and S wave ultrasonic signals, examples of which will be provided in the results section.

An interactive software routine was developed to calculate attenuation using a spectral ratio technique described by Toksoz et al. (1979). In the experimental procedure, two signals were recorded with the equipment settings exactly the same, one through the rock and the second through the aluminum standard of the same dimensions. With the computer the digitized signals were displayed and windowed in the time domain over approximately 1.5 to 2 full cycles. The window edges were smoothed with a cosine taper. The two windowed signals were decomposed into amplitude versus frequency data utilizing standard Fourier analysis. The individual amplitude data and the logarithm of the ratio between them were displayed as a function of frequency. A least squares fit of the slope was made over a frequency band defined interactively. The inverse quality factor Q^{-1} was calculated by multiplying the slope, in units of time, with sample velocity, and dividing by the sample length times pi (π).

This method of measuring and calculating attenuation requires several assumptions. Attenuation is assumed to be constant over the frequency band of the signal, geometrical

factors such as spreading and reflections are assumed constant for the two signals, and attenuation of the aluminum is taken as very small relative to the rock. An important variable in applying the technique included variations in window lengths, both in the time domain over which the ultrasonic signal was selected and in the frequency domain over which the spectral ratio slope was taken. A conservative estimate of error in applying the technique is $\pm 20\%$.

EXPERIMENTAL RESULTS

Hysteresis Loop

Table 1 contains the results of hysteresis loop attenuation measurements on the room dry and water-saturated cylinder of Sierra White granite. The five columns list the frequency, strain amplitude, saturation, Young's modulus in GPa, and extensional attenuation ($1000/Q_e$). The strain amplitude is the maximum peak to peak amplitude of the recorded displacement signal divided by the ring separation. The Young's modulus is calculated from the corresponding axial stress that was recorded.

The hysteresis loop for the dry sample is shown in Figure 4. In this plot the horizontal axis is strain in units of microstrain and the vertical axis is stress in units of MPa times ten. This hysteresis loop was averaged from 128 cycles of sinusoidal stress applied to the sample end at a frequency of 0.1 Hz. The time sequence of stress and strain follows the hysteresis loop in a clockwise rotation, so that as the stress is reversed the strain lags behind and forms the loop. The extensional attenuation factor was obtained by directly measuring the phase angle between the original sinusoidal signals with Fourier analysis.

Resonant Bar

Table 2 contains the result of resonant bar measurements on the dry and saturated sample of Sierra White granite. In the table are columns of center resonant frequency, the harmonic of the resonance, the saturation, Young's modulus in GPa, and extensional attenuation ($1000/Q_e$). Young's modulus was calculated from the square of the extensional velocity times the density. The fundamental resonance peak and the 8th harmonics for the dry and saturated sample are shown in Fig. 5. While the center frequencies of the two resonances are nearly the same, the much greater attenuation for the saturated sample is indicated by the broad width of the resonance. The higher harmonics tended to be distorted, and the highest frequency for the water saturated measurements was limited by this distortion. The highest frequency for the dry measurements was limited by the upper

frequency capacity of the phase-lock amplifier.

Ultrasonic

Table 3 contains the results of the benchtop ultrasonic velocity and attenuation measurements on Sierra White granite samples. The measurements are grouped vertically in the table according to the spectral bandwidth of the ultrasonic transducers, with the highest frequency (0.6 - 1.1 MHz) at the top, followed by the intermediate frequency (100 - 200 kHz), and lowest frequency (40 - 80 kHz) at the bottom. The columns identify the spectral bandwidth of the paired ultrasonic transducers, a number code for the sample that is explained at the table bottom, the saturation, P and S wave velocities in km/s, Young's modulus in GPa, and the compressional (P), shear (S), and extensional (e) attenuations ($1000/Q$). The equivalent ultrasonic Q_e^{-1} was computed in order to compare the Q_p^{-1} and Q_s^{-1} measured in the ultrasonic wave propagation experiments with the Q_e^{-1} measured in the resonant bar and hysteresis loop experiments. If the material is assumed to be isotropic and the attenuation is small, then complex moduli can be substituted for real moduli in linear elasticity relations and the following relationship follows (Winkler and Nur, 1979):

$$(1-\nu)(1-2\nu)Q_p^{-1} = (1+\nu)Q_e^{-1} - 2\nu(2-\nu)Q_s^{-1}$$

where ν is Poisson's ratio.

P and S wave velocities and attenuations were also measured for the smaller 0.15 m Sierra White granite sample as a function of confining pressure for both the dry and water saturated conditions. The P and S wave velocity data are presented in Figure 7 and the calculated P, S, and e attenuations ($1000/Q$) are shown in Figure 8.

Discussion

The experimental data on Sierra White granite determined with the hysteresis loop, resonant bar, and ultrasonic techniques provide a good basis for observations and comparisons concerning the effects of frequency, saturation, pressure, and experimental technique on attenuations and moduli. Multiple experiments were conducted on oriented samples prepared from the same original block of Sierra White granite. A broad range of frequencies from 0.1 Hz to 1 MHz, were investigated, and there was partial overlap of frequencies between 100 to 200 kHz for resonant bar and ultrasonic measurements. Dry and water saturated results were obtained with all of the techniques. Finally, the pressure dependence of attenuation to 100 MPa was also determined with dry and saturated ultrasonic measurements in the 0.6 - 1.1 MHz frequency band.

The attenuation and moduli data for the dry samples in Tables 1, 2, and 3 show surprisingly good agreement for Young's modulus but a complicated result for attenuation. The Young's modulus measurements range from 33.8 to 35.2 GPa for the hysteresis loop, the fundamental resonance of the resonant bar, and the ultrasonic P and S wave measurements over two frequency bands (100-200 kHz and 0.6 - 1.1 MHz). No monotonic trend exists as a function of frequency, and the 4% variation can be considered as part of experimental error. Although desirable, modulus dispersion over the broad frequency range cannot be accurately established with this data due to limitations of experimental precision and sample variability.

The non-ultrasonic extensional attenuations are comparable for the dry samples, with the hysteresis loop Q_e^{-1} equal to 0.0083 and the resonant bar value equal to 0.00526 at the fundamental resonance. Between the fundamental (10.436 kHz) and the 3rd harmonic of the fundamental (39.894 kHz) resonant bar attenuation monotonically increases to 0.00662, then at higher harmonics only varies between 0.00616 and 0.00795. The corresponding Young's modulus data for the harmonics decrease between the fundamental and 3rd harmonic, and thereafter shows random variations between 31.5 and 33.6 GPa. Some of the negative modulus dispersion between the fundamental and 3rd harmonic may be due to geometrical effects, which would also contribute to higher Q_e^{-1} , but it is not clear why the trend apparently stops at the 3rd harmonic.

In contrast with the hysteresis loop and resonant bar results, the ultrasonic experiments show that there is a strong dependence of attenuation on frequency (Table 3). For the dry Sierra White granite samples the three ultrasonic P-wave attenuations ($1000/Q_p$) at 0.6 - 1.1 MHz, 100-200 kHz, and 40-80 kHz were 0.065, 0.028, and 0.020, respectively. Therefore the P-wave attenuation in the highest frequency band was over three times greater than in the lowest frequency band. Similarly, S-wave attenuation ($1000/Q_s$) in the 0.6 - 1.1 MHz frequency band was 0.047, or approximately four and one-half times greater than the 0.011 value measured in the 100-200 kHz band. The calculated extensional attenuations ($1000/Q_e$) were 0.058 and 0.024 in the same corresponding frequency bands.

The frequency dependence of ultrasonic attenuation raises a number of questions. First, it obviously negates the assumption in the spectral ratio calculation that attenuation is constant over the spectral bandwidth of the pulse. Therefore the given attenuations must be treated as estimates for the limited bandwidths over which the spectral ratio was taken. Second, the trend implies that frequency-dependent scattering is probably an important attenuation mechanism for ultrasonic pulses at these frequencies.

A particularly interesting feature of the ultrasonic and resonant bar results for the dry samples is the overlap in frequency from approximately 100 to 200 kHz (Tables 2 and 3). As discussed previously, the Young's modulus data from the two techniques are equivalent to within experimental error. The calculated ultrasonic Q_e^{-1} of 0.024 is, however,

approximately three to four times larger than the resonant bar Q_e^{-1} , which range from 0.0065 to 0.008 for the higher harmonics in the same frequency band. In addition, resonant bar attenuations to the 20th harmonic (212 kHz) on the dry sample show no clear trend for attenuation changing with frequency. Therefore, a fundamental disagreement exists between the attenuations measured with the ultrasonic and resonant bar techniques. The difference may decrease for the water saturated samples. Although ultrasonic measurements on saturated samples were not made with the 100-200 kHz transducers, the difference would probably be reduced by the proportionally larger increase in resonant bar attenuation upon saturation. The difference may also decrease at lower frequencies. The trend for dry P-wave ultrasonic attenuations is down for decreasing frequencies (Table 3), and at some frequency lower than 50 kHz the resonant bar and pulse attenuations may agree. The reasons for the difference between ultrasonic and resonant bar attenuations are not entirely clear. One possibility is that the scattering attenuation mechanism that elevates ultrasonic pulse attenuations does not operate equally on the standing waves in an extensional resonant bar experiment.

The effect of water saturation on attenuation and moduli in Sierra White granite also contrasts the hysteresis loop and resonant bar results with the ultrasonic pulse results. In the hysteresis loop experiment, water saturation caused Young's modulus to decrease from 33.8 to 31.2 GPa and Q_e^{-1} to increase dramatically from 0.0083 to 0.026 (Table 1). Similarly, in the resonant bar experiment, water saturation caused a large increase of Q_e^{-1} from 0.00526 to 0.0397 at the fundamental resonance and only a slight increase in Young's modulus, from 35.2 to 35.3 GPa, a change that is within the experimental error. Both attenuation and Young's modulus decreased at higher harmonic resonances, however, with attenuation dropping to 0.0255 and Young's modulus to 31.8 GPa at the 8th harmonic. In summary, saturation causes a slight decrease in Young's modulus at the lower frequency, no change at the fundamental (10.4 kHz) frequency, and increases by a factor of three and a factor of seven and one-half the extensional attenuation for the hysteresis loop and resonant bar attenuations, respectively.

The large attenuations associated with saturation can be interpreted as a results of viscous fluid flow within thin microcracks and pores of the granite. Two dissipation mechanisms are possible with fluid flow. The rest is inertial shear between crack surfaces and bulk pore fluid (Biot, 1956a,b). The energy loss associated with this mechanism, however, is very small in a low-porosity granite at sub-ultrasonic frequencies. The second mechanism is viscous loss within pore fluid due to pressure gradients between adjacent pore volumes induced by dynamic elastic deformation. This mechanism has received considerable attention (O'Connell and Budiansky, 1977; Mavko and Nur, 1979; Murphy, 1982; Bulau et al., 1984) but specific models of pore distributions and pressure gradients have not been developed.

The ultrasonic pulse results, on the other hand, probably combine fluid flow losses with scattering. In the 0.6 - 1.1 MHz frequency band Q_s^{-1} and Q_e^{-1} increase upon saturation (Table 3), although not nearly as much as at lower frequencies. This can be interpreted as a fluid flow related attenuation mechanism. The Q_p^{-1} , however, actually decreases upon saturation, an observation that correlates well with a scattering mechanism. Winkler (1983) has concluded that scattering is quite prevalent in sandstones at ultrasonic frequencies. His calculations of the scattering cross-section of a dry and saturated single spherical scatterer indicate that the dry case will result in approximately twice the scattering loss of a fluid-filled scatterer. The measured reduction of Q_p^{-1} upon saturation agrees with the sign of the calculation but not quite the magnitude, probably because scattering is combined with viscous fluid loss. In the 40-80 kHz frequency band the reverse effect is observed. The water saturated Q_p^{-1} (0.064) is much larger than the dry (0.020). At these lower frequencies fluid flow loss may dominate over scattering loss.

Confining pressure closes or reduces the size of microcracks, increasing ultrasonic velocities and reducing attenuations (Figures 7 and 8). The dry and saturated properties also converge with increasing pressure. The microcrack population responsible for the P wave scattering is apparently removed by the application of 45 MPa of effective confining pressure. The convergence of dry and saturated attenuations also indicates that the fluid flow mechanism is reduced as thin microcracks close under pressure. At the highest confining pressure the minimum extensional attenuation is 0.022, which is still a factor of 3 to 4 times greater than the dry hysteresis loop and resonant bar attenuations. Ultrasonic scattering may therefore still occur at high pressures because microcracks do not close entirely.

The experimental data in this study is graphically summarized in Figures 9 and 10 along with several sets of previous experimental results. These plots give the extensional mode attenuations ($1000/Q_e$) versus log frequency for dry (Fig. 9) and saturated (Fig. 10) Sierra White granite obtained in this study plus pertinent results on various other granites. The hysteresis loop, resonant bar, and ultrasonic pulse data are labelled in each plot. The results of others are number-coded according to the key in the figure caption. Spencer (1981) and Liu and Peselnick (1983) conducted experiments with the hysteresis loop technique on Oklahoma and Westerly granites, respectively. Spencer collected data on a vacuum dry sample as a function of frequency from approximately 5 Hz to 400 Hz, and the solid line in Fig. 9 represents an upper bound for the data he collected. The Q_e^{-1} reported by Liu and Peselnick (1983) on a room dry sample have been increased by a factor of 4 (discussed in the first section of this report). Also included in these plots are resonant bar results by Murphy (1984) and Winkler et al. (1979) on Sierra White granite, Gordon and Davis (1968) on Tupper Lake granite, Johnston and Toksoz (1980) and Tittmann (1984) on Westerly granite. These attenuation data are all Q_e^{-1} except for Tittmann's results,

which are Q_s^{-1} collected in the flexural and torsional modes.

The attenuation data in Fig. 9 for room dry granite specimens are fairly well clustered between 0.005 and 0.010 (Q_e^{-1}) at frequencies from 0.1 Hz to the highest frequency resonant bar experiment (212 kHz). These data include the hysteresis loop and resonant bar experiments, plus the results of Liu and Peselnick (1983), Tittmann (1984), Winkler et al. (1979), and Johnston and Toksoz (1980) on Westerly and Sierra White granites. Collectively, the data indicate a lack of frequency dependence for attenuation in these room dry granites, and surprisingly good agreement between the hysteresis loop and resonant bar measurements.

Attenuation in nominally "dry" rock is closely related to moisture content and microcrack population. An experimentally measured Q^{-1} of 0.1 for a basalt exposed to high-humidity air can be reduced to 2×10^{-4} by following a strong outgassing procedure Tittmann (1977). In addition, Spencer (1981) showed that hysteresis loop attenuation measurements for vacuum dry samples are similarly very low. The line segment associated with Spencer (1981) in Fig. 9 is actually an upper bound for many measurements on Oklahoma granite that were much closer to zero attenuation. The severe attenuation caused by small amounts of surface adsorbed water is probably a combination of viscoelastic and electrostatic responses to stress by thin water layers in the microcracks of what are otherwise "dry" rocks (Bulau et al., 1984). Therefore, the clustering of Q_e^{-1} factors between 0.005 and 0.010 is a reflection of typical microcrack populations for these granites and laboratory ambient humidities.

The attenuation factors for the water-saturated granites (Fig. 10) are substantially larger than for the dry samples and exhibit a complicated dependence on frequency. A Q_e^{-1} of 0.026 was measured by the hysteresis loop experiments at 0.1 Hz, approximately three times greater than for the dry sample. A greater increase was also measured and a resonant bar experiments, although between 10 kHz and 90 kHz Q_e^{-1} is decreasing as a function of increasing frequency.

The experiments on Sierra White granite reported in this paper are consistent with, but do not fully confirm, a broad relaxation peak in the extensional mode attenuation spectrum for saturated rocks reported by Spencer (1981). The dashed line in Fig. 10 outlines the shape of the relaxation peak with a center frequency of around 1 kHz. The flanks of the peak are partially defined by Spencer's (1981) hysteresis loop data between 5 and 400 Hz for Oklahoma granite, and the resonant bar data between 10 and 90 kHz for Sierra White granite. Murphy's (1984) resonant bar data on Sierra White granite apparently fall close enough to the relaxation peak so as to not exhibit dependence of attenuation on frequency. The hysteresis loop data at 0.1 Hz is also consistent with the relaxation peak, but the ultrasonic Q_e^{-1} may be high due to scattering. The Davis and Gordon (1968) data point on saturated Tupper Lake granite is somewhat high, as it was for the dry sample, but still

roughly follows a trend of decreasing attenuation at the higher frequencies. The only serious discrepancy is found in the torsional and flexural attenuations on Westerly granite by Tittmann (1984), which are well below all of the other data. The reason for this is not clear, although shear attenuation should be similar to or greater than extensional mode attenuation (Murphy, 1984; Winkler and Nur, 1979).

The relaxation peak and elevated attenuation for the saturated granites can be generally explained by attenuation mechanisms based on viscous fluid flow within the microcracks in response to a propagating stress wave (O'Connell and Budiansky, 1977; Mavko and Nur, 1979). An additional attenuation mechanism suggested by Spencer (1981), based on his analysis of the effects of various saturants on the relaxation peak and Young's modulus, is the dynamic response of chemical bonds between saturating fluid and mineral surfaces. Either dissipation process results in a peak in the attenuation spectrum, with a transition from lower moduli at frequencies below the center frequency to higher unrelaxed moduli at frequencies above the center frequency. The resonant bar results in this study, however, show that saturated Young's moduli are not much larger than the saturated hysteresis loop value, and not nearly that predicted by Spencer (1981) in this Cole-Cole distribution of relaxation times. One possible explanation is that the unjacketed resonant bar may have only been partially saturated during the saturated experiment, resulting in a lower Young's modulus.

Further experimental investigations utilizing all three techniques are warranted in order to fully document and interpret attenuation in granite. In this study the ultrasonic pulse technique was applied in three frequency bands, from 100 to 200 kHz and 0.6 to 1.1 MHz for both P and S waves, and from 40 to 80 kHz for the P wave. Although ultrasonic attenuations are large, particularly for dry samples, attenuation is clearly decreasing at lower frequencies. A suitable S wave transducer in the 40-80 kHz band needs to be developed, and dry and water saturated data at these lower frequencies are desirable. At some frequency the unrelaxed ultrasonic modulus and attenuation should decrease and agree with the hysteresis loop and resonant bar data. An understanding of the scattering attenuation mechanism and attenuation spectra for these ultrasonic pulses in intact rock may provide some insight into the larger-scale scattering phenomena that occur at seismic frequencies in the earth's crust.

The relaxation peak that is postulated to occur around 1 kHz for the saturated granite requires further definition. The results of Spencer (1981) and Bulau et al. (1984) show an increase of attenuation towards 1 kHz; the data collected on Sierra White granite displays a corresponding decrease in the resonant bar data at frequencies from 10 to 90 kHz. The resonant bar technique may be used for a complete frequency sweep through the relaxation peak by reducing the fundamental resonance, either through loading, in the manner of Tittmann (1984), or with longer samples. In order to obtain fundamental resonant frequency of around 1 kHz samples on the order of 1.7 meters long would have to be

prepared. At low frequencies, on the opposite side of the relaxation peak, the hysteresis loop technique can be performed over a broader frequency band, in the manner developed by Spencer (1981). This would fill in the frequency dependence over the seismic frequency band and better define the relaxation peak.

Conclusions

In this study a comparison has been made of the moduli and attenuations for dry and saturated Sierra White granite determined with the hysteresis loop, resonant bar, and ultrasonic techniques. The hysteresis loop and resonant bar results indicate that for room-dry granite the Young's modulus and extensional attenuation are nearly constant over a broad frequency range from 0.1 Hz to at least 200 kHz. Water saturation caused a dramatic increase in extensional attenuation, by factors of four to seven and one-half, but had a minimal effect on Young's modulus. In addition, resonant bar attenuations in the range 10-90 kHz decreased with increasing frequency, consistent with a relaxation peak in the extensional attenuation spectra at a frequency below 10 kHz. The attenuation mechanism is viscous fluid flow within the microcracks of the granite.

Ultrasonic attenuations and moduli in three different frequency bands show that scattering is probably an important attenuation mechanism at these frequencies. Although the dry Young's moduli derived from P and S wave velocities agree with the resonant bar and hysteresis loop moduli, in the 100-200 kHz frequency band the ultrasonic Q_e^{-1} is larger than the resonant bar values by a factor of 3 to 4. Scattering is also manifested in the effects of saturation on attenuation. The water saturated Q_p^{-1} at 0.6 - 1.1 MHz is less than dry because the effective cross-sectional area of the scattering cracks is probably reduced by the presence of fluid. The scattering mechanism also combines with fluid losses, however, because Q_e^{-1} and Q_s^{-1} increase in the saturated sample at 0.6 - 1.1 MHz. Confining pressure closes or reduces the size of microcracks, increasing velocities and reducing attenuation. At high pressures the dry and saturated velocities and attenuations converge.

The three experimental techniques, hysteresis loop, resonant bar, and ultrasonic, each have characteristics that can be uniquely applied to various requirements for measuring and documenting dynamic properties of rock. From the seismological perspective the most desirable and relevant laboratory determinations would utilize hysteresis loops because the frequency bandwidths are comparable. Since the cyclic stress can be varied to any desired amplitude, large strain-amplitude measurements can also be made, even to near failure. In addition, large samples can be used for investigating larger scale inhomogeneities such as fractures. On the other hand, the technique is experimentally difficult and loses resolution at very low attenuations. Ultrasonic attenuations are probably dominated by scattering

mechanisms. Although the exact attenuation values may not be particularly relevant to lower frequencies, scattering phenomena at lower frequencies may perhaps be studied. Resonant bar experiments have the greatest resolution at very low attenuations. In addition, they may be conducted under confining pressure and with different saturations. In addition to the extensional resonance experiments performed in this study, complimentary torsional or flexural shear measurements may also be made. Resonant bar measurements are probably a suitable compromise for dry measurements, given the lack of frequency dependence for dry samples below ultrasonic frequencies.

REFERENCES

Biot, M.A., 1956a, Theory of propagation of elastic waves in a fluid-saturated porous solid - I. Low frequency range: *J. Acoust. Soc. Am.*, 28, 168-178.

Biot, M.A., 1956b, Theory of propagation of elastic waves in a fluid-saturated porous solid - II. Higher frequency range: *J. Acoust. Soc. Am.*, 179-191.

Brennan, B.J., and F.D. Stacey, Frequency dependence of elasticity of rock-test of seismic velocity dispersion, *Nature*, 268, 220-222, 1977.

Brennan, B.J., Linear viscoelastic behavior in rocks, in *Anelasticity in the Earth, Geodyn. Ser.*, vol. 4, edited by F.D. Stacey, M.S. Paterson, and A. Nicolas, pp. 13-22, AGU, Washington, D.C., 1981.

Bulau, J.R., B.R. Tittmann, M. Abdel-Gawad, and C. Salvado, The role of aqueous fluids in the internal friction of rock, *J. Geophys. Res.*, 89, 4207-4212, 1984.

Clark, V.A., B.R. Tittman, and T.W. Spencer, Effects of volatile on attenuation (Q^{-1}) and velocity in sedimentary rocks, *J. Geophys. Res.*, 85, 5190-5198, 1980.

Coyner, K.B., Attenuation measurements on dry Sierra White granite, dome salt, and Berea sandstone, final report to Lawrence Livermore National Laboratory, Contract #9092405, 1987.

Gordon, R.B., and L.A. Davis, Velocity and attenuation of seismic waves in imperfectly elastic rock, *J. Geophys. Res.*, 73, 3917-3935, 1968.

Jackson, I., M.S. Paterson, H. Niesler, and R.M. Waterford, Rock anelasticity measurements at high pressure, low strain amplitude and seismic frequency, *Geophysical Research Letters*, 11 1235-1238, 1984.

Johnston, D.H., and M.N. Toksoz, Thermal cracking and amplitude dependent attenuation, *J. Geophys. Res.*, 85, 937-942, 1980.

Liu, H.-P., and L. Peselnick, Investigation of internal friction in fused quartz, steel, plexiglas, and Westerly granite from 0.01 to 1.00 Hertz at 10^{-8} to 10^{-7} strain amplitude, *J. Geophys. Res.*, 88, 2367-2379, 1983

Mavko, G., and A. Nur, Wave attenuation in partially saturated rocks, *Geophys*, 44, 161-178, 1979.

McKavanagh, B., and F.D. Stacey, Mechanical hysteresis in rocks at low strain amplitudes and seismic frequencies, *Physics of the Earth and Planetary Interiors*, 8, 46-250, 1974.

Minster, J.B., and S.M. Day, Decay of wave fields near an explosive source due to high-strain, nonlinear attenuation, *Journal of Geophysical Research* 91, 2113-2122, 1986.

Murphy, W.F., Effects of partial water saturation on attenuation in Massillon sandstone and Vycor porous glass, *J. Acoust. Soc. Am.*, 71, 1458-1468.

O'Connell, R.J., and B. Budiansky, Viscoelastic properties of fluid-saturated cracked solids, *J. Geophys. Res.*, 82, 5719-5736, 1977.

Peselnick, L., and W.F. Outerbridge, Internal friction in shear and shear modulus of Solenhofen limestone over a frequency range of 10^7 cycles per second, *J. Geophys. Res.*, 66, 581-588, 1961.

Spencer, J.W., Stress relaxations at low frequencies in fluid-saturated rocks: Attenuation and modulus dispersion, *J. Geophys. Res.*, 86, 1803-1812, 1981.

Tittmann, B.R., Internal friction measurements and their implications in seismic Q structure models of the crust, in *The Earth's Crust: Monograph 20*, AGU, 197-213, 1977.

Tittmann, B.R., Nonlinear wave propagation study, semi-annual technical report No. 2 for the period December 1, 1983 through May 31, 1984, SC5361.6SAR, Rockwell International Science Center, 1984.

Toksoz, M.N., D.H. Johnston, and A. Timur, Attenuation of seismic waves in dry and saturated rocks, I, Laboratory measurements, *Geophys*, 44, 681-690, 1979.

Walsh, J.B. Seismic wave attenuation in rock due to friction, *J. Geophys., Res.*, 71, 2591-2599, 1966.

Walsh, J.B., W.F. Brace, and W.R. Wawersik, Attenuation of stress waves in Cedar City quartz diorite, Technical Report No. AFWL-TR-70-8, M.I.T., 1970.

Winkler, K.W., A. Nur, and M. Gladwin, Friction and seismic attenuation in rocks, *Nature*, 277, 528-531, 1979.

TABLE 1. Attenuation measurements in Sierra White granite utilizing the hysteresis loop technique.

FREQUENCY	STRAIN AMPLITUDE MICROSTRAIN	SATURATION	YOUNG'S MODULUS (GPa)	ATTENUATION (1000/Q _e)
0.1 Hz	0.50	Dry	33.8	8.3
	1.92	Water	31.2	26.0

TABLE 2. Attenuation measurements in Sierra White granite utilizing the resonant bar technique.

FREQUENCY (kHz)	HARMONIC	SATURATION	YOUNG'S MODULUS (GPa)	ATTENUATION (1000/Qe)
10.436	0	Dry	35.2	5.26
20.600	1	Dry	34.3	5.65
30.462	2	Dry	33.3	6.11
39.894	3	Dry	32.2	6.62
50.064	4	Dry	32.4	6.16
59.843	5	Dry	32.2	6.29
69.135	6	Dry	31.5	6.70
80.048	7	Dry	32.4	6.56
90.245	8	Dry	32.5	6.50
101.252	9	Dry	33.2	7.15
110.824	10	Dry	32.8	6.70
121.804	11	Dry	33.3	7.38
132.567	12	Dry	33.6	6.61
141.595	13	Dry	33.1	7.45
152.075	14	Dry	33.2	7.95
161.999	15	Dry	33.2	6.80
171.243	16	Dry	32.8	7.54
181.654	17	Dry	32.9	7.31
192.130	18	Dry	33.1	7.00
102.797	19	Dry	32.9	6.72
211.928	20	Dry	32.9	6.51
10.455	0	Water	35.3	39.7
20.534	1	Water	34.1	35.7
30.435	2	Water	33.3	35.9
40.902	3	Water	33.8	29.1
49.892	4	Water	32.2	30.7
59.251	5	Water	31.5	26.8
68.478	6	Water	30.9	26.8
70.050	7	Water	31.6	23.0
89.262	8	Water	31.8	25.5

TABLE 3. Attenuation measurements in Sierra White granite utilizing the ultrasonic pulse technique.

FREQ.	SAM.	SAT.	VELOCITY (km/sec)		YOUNG'S MODULUS (GPa)	ATTENUATION (1000/Q)		
			P WAVE	S WAVE		P	S	E
0.6-1.1 MHz	1	Dry	3.686	2.434	34.8	65	47	58
		Water	5.444	3.127	64.7	46	87	75
100-200 kHz	2	Dry	3.593	2.454	33.8	28	11	24
40-80 kHz	3	Dry	3.536			20		
		Water	5.331			64		

Samples: 1 = 0.152 m long cylinder, 2 = 0.203 m thick block, 3 = 0.508 m long cylinder

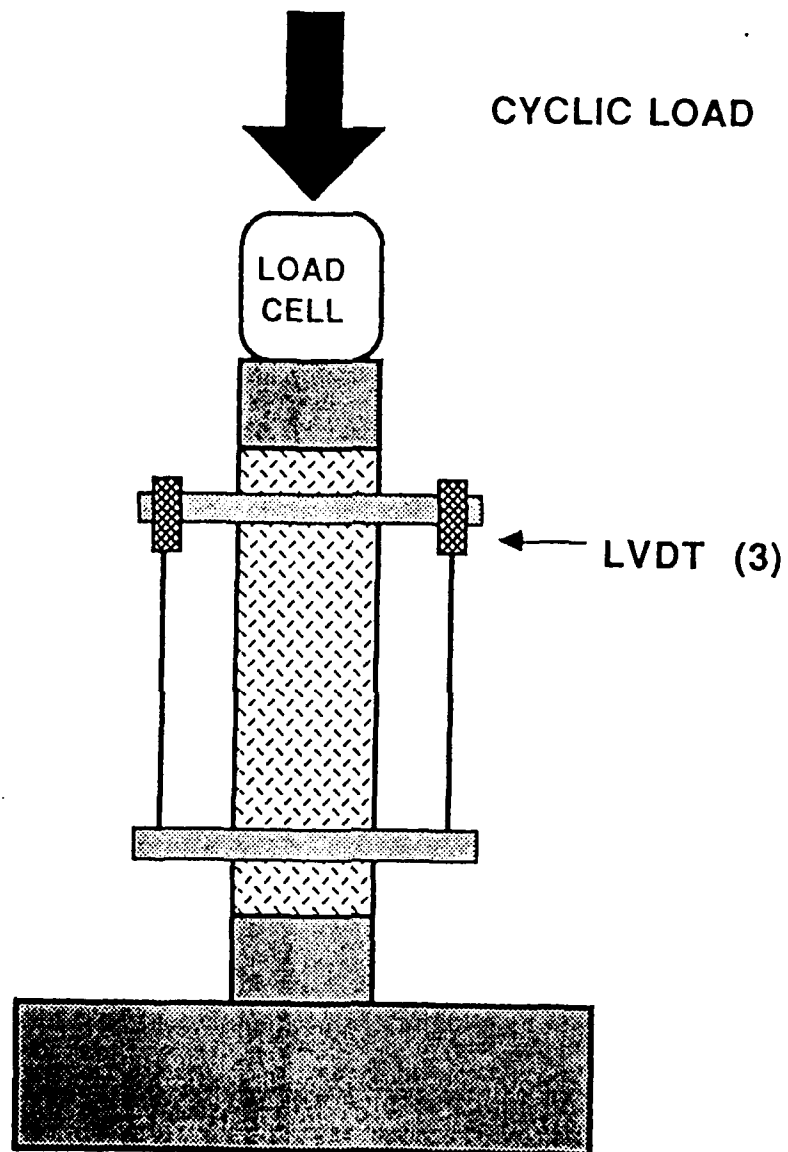


Figure 1. Schematic diagram of the experimental apparatus for low frequency hysteresis loop attenuation measurements.

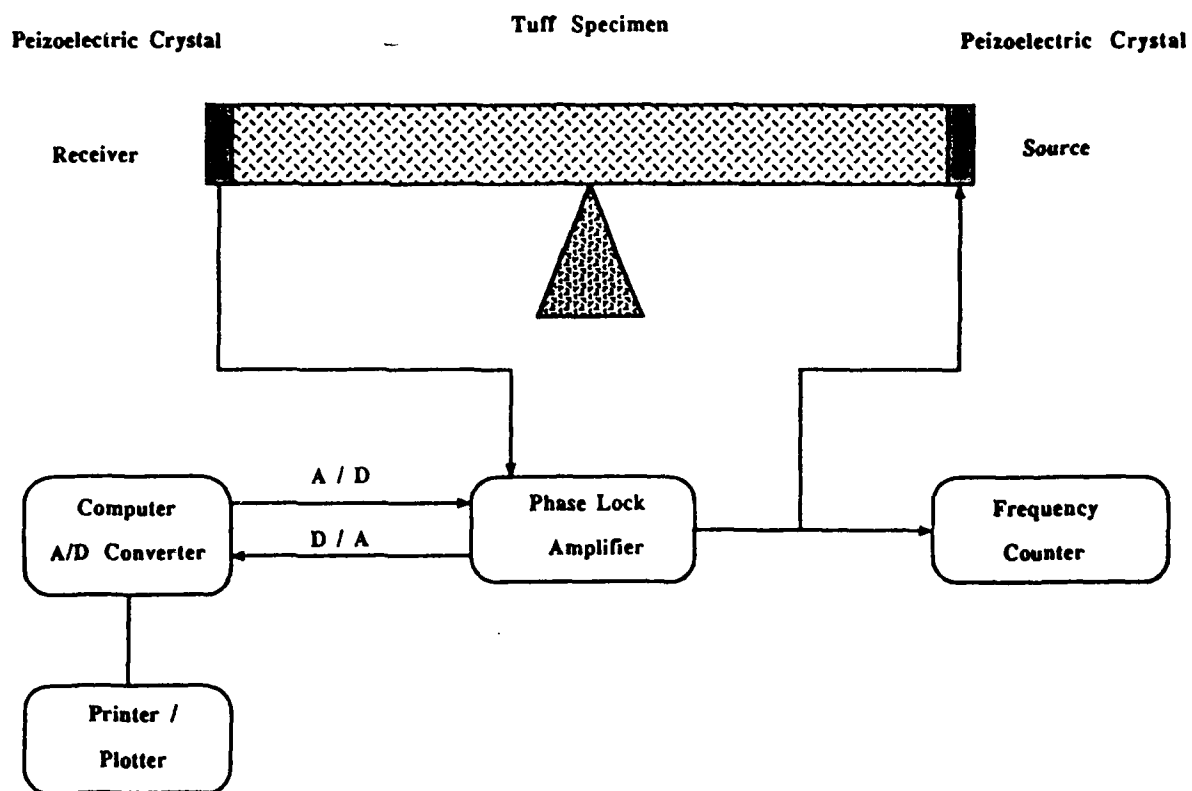


Figure 2. Schematic diagram of the benchtop resonant bar apparatus.

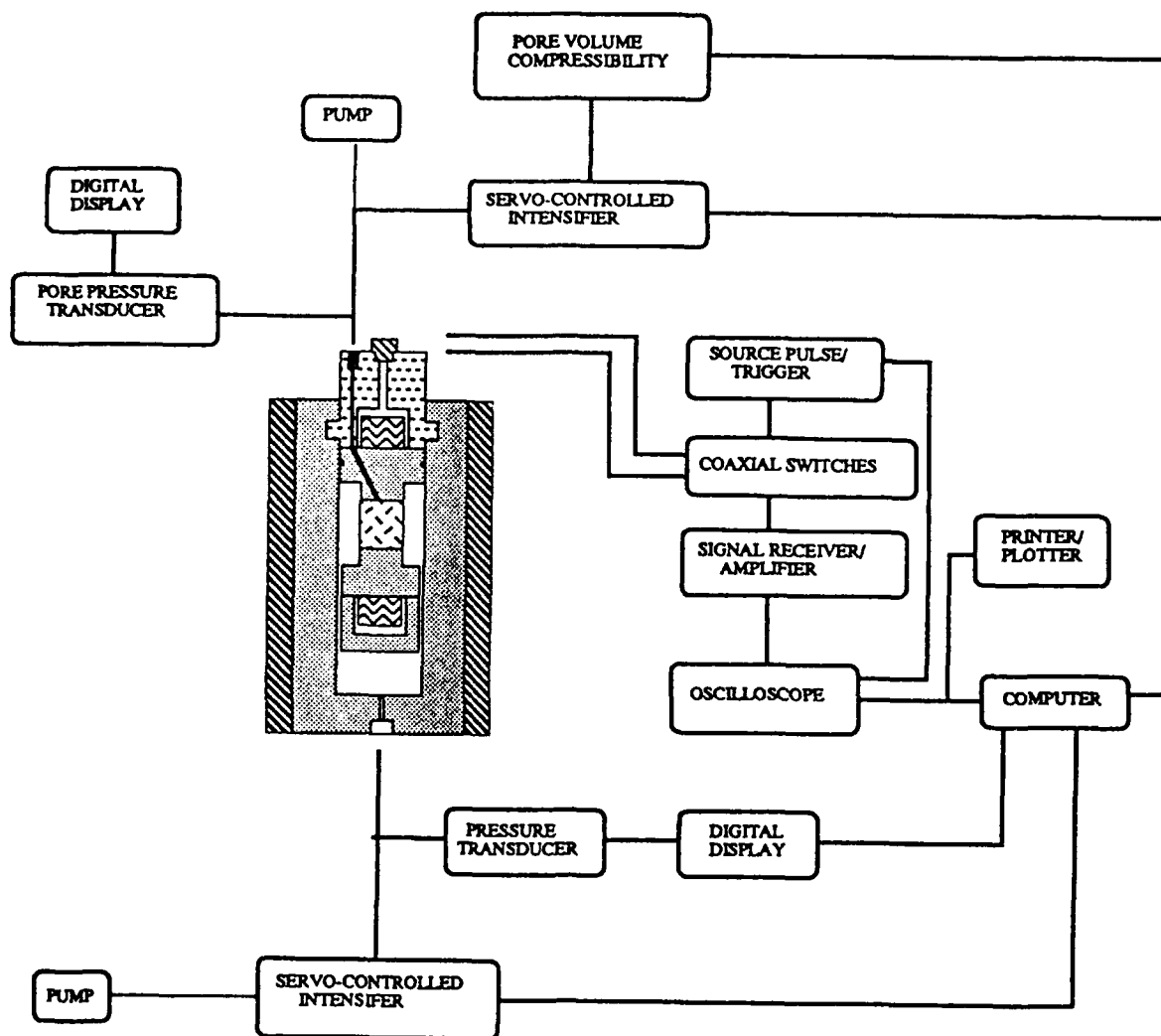


Figure 3. Schematic diagram of the experimental apparatus for ultrasonic velocity and attenuation measurements under pressure.

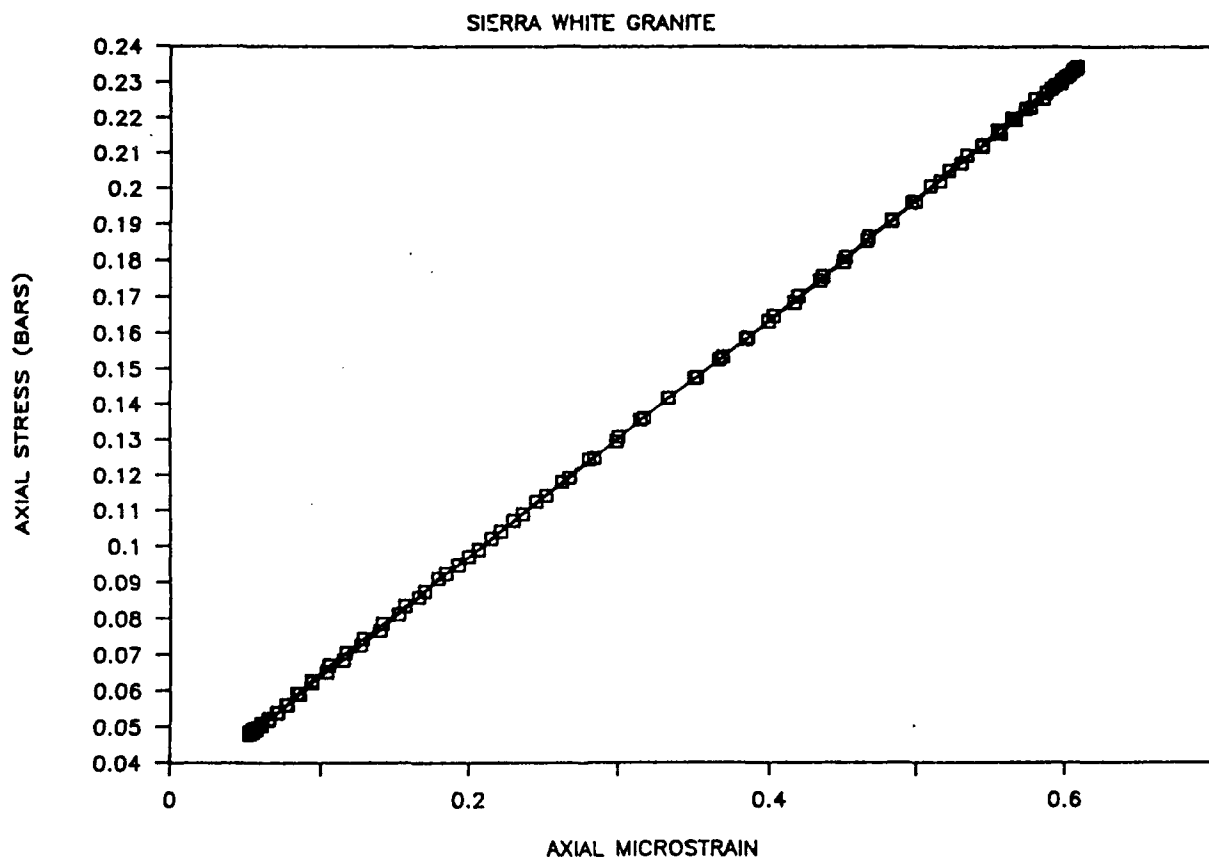


Figure 4. Hysteresis loop for dry Sierra White granite at a strain amplitude of 0.56 microstrain. The vertical scale is axial stress in MPa. The attenuation factor calculated for this sample is 0.0083.

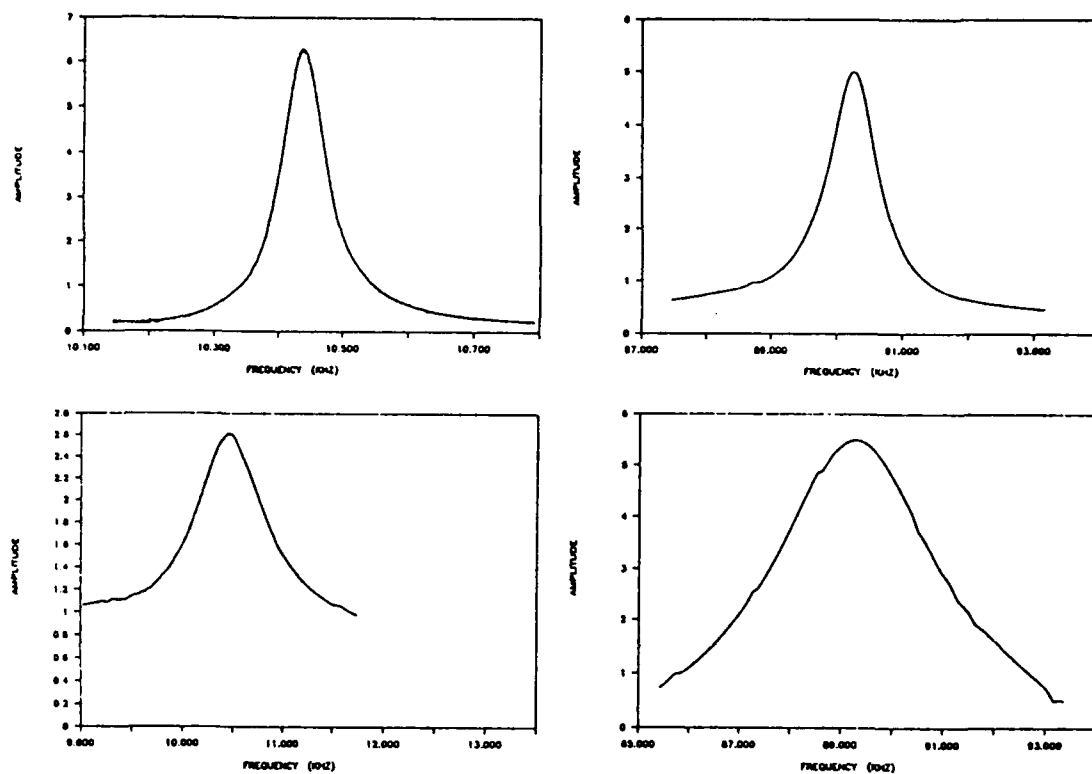


Figure 5. Fundamental (left) and 8th harmonic (right) extensional resonance for room-dry (top) and water saturated (bottom) Sierra White granite.

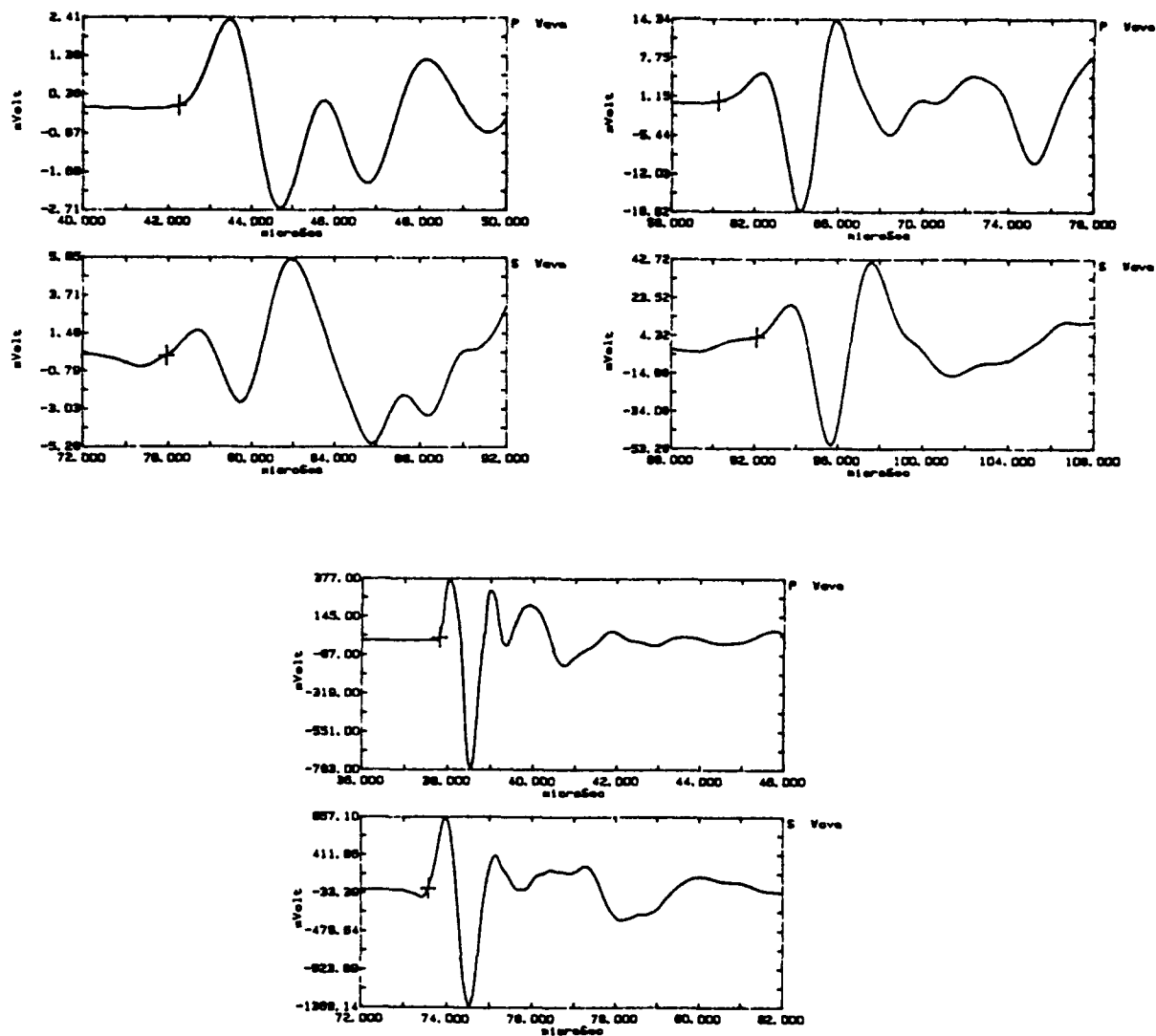


Figure 6. Ultrasonic (0.6-1.1 MHz) P- and S-wave signals propagated through the 0.152 m sample of dry (upper left) and water saturated (upper right) Sierra White granite and through the 0.15 m aluminum standard (bottom).

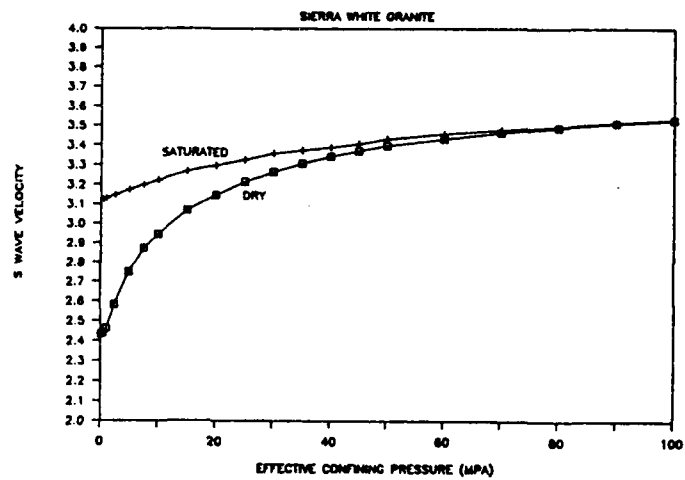
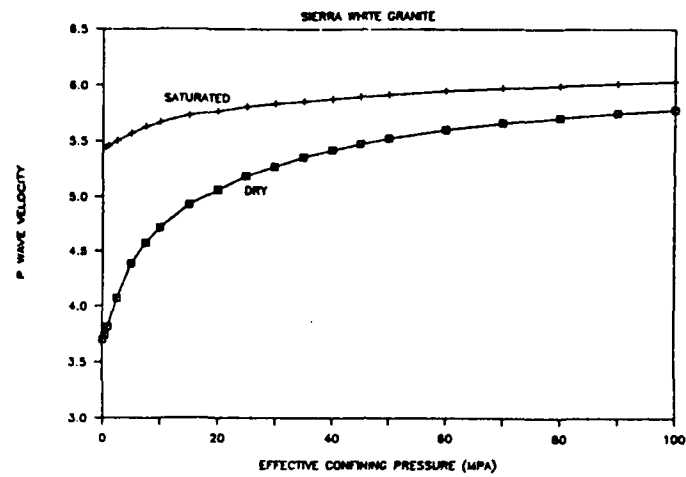


Figure 7. P and S wave velocities for dry and water saturated Sierra White granite measured as a function of confining pressure.

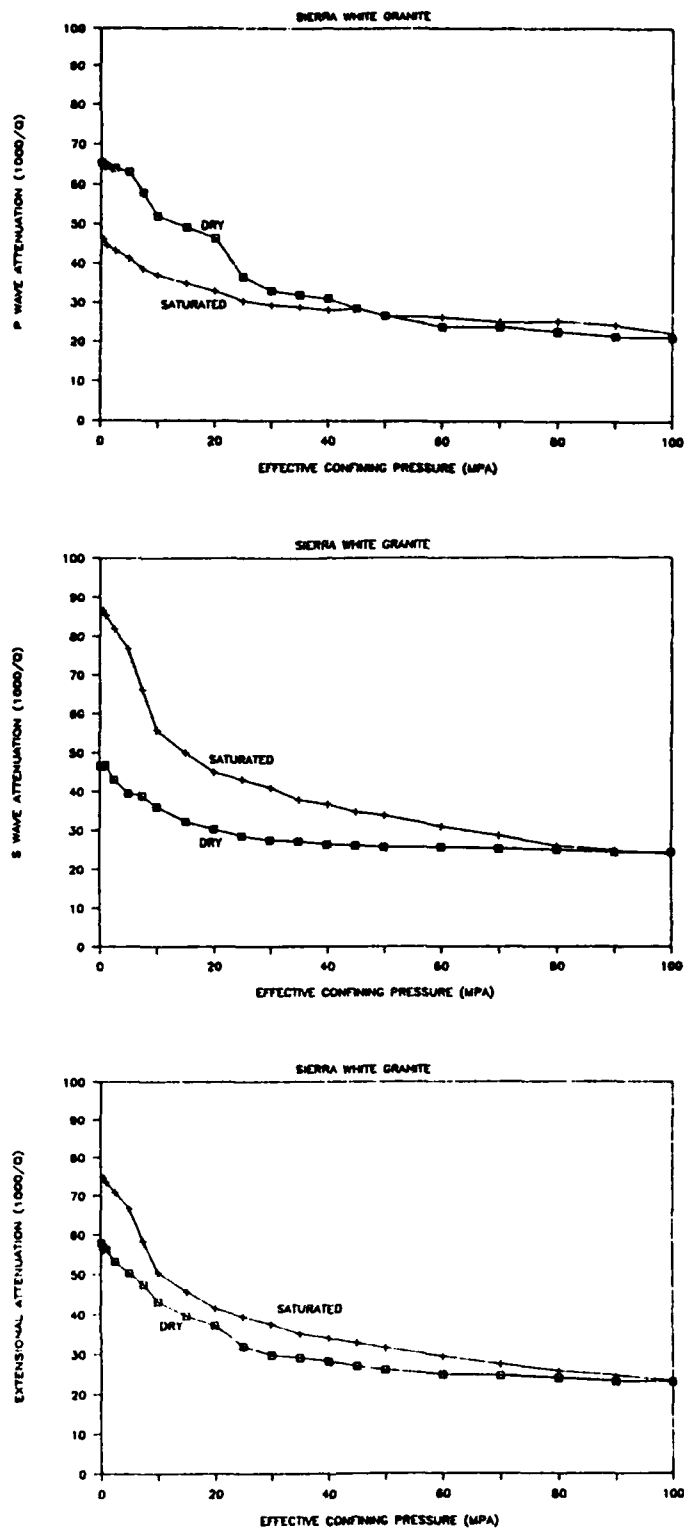


Figure 8. Ultrasonic (0.6 - 1.1 MHz) P and S wave attenuation, and calculated extensional attenuation (1000/Q), for dry and water saturated Sierra White granite measured as a function of confining pressure.

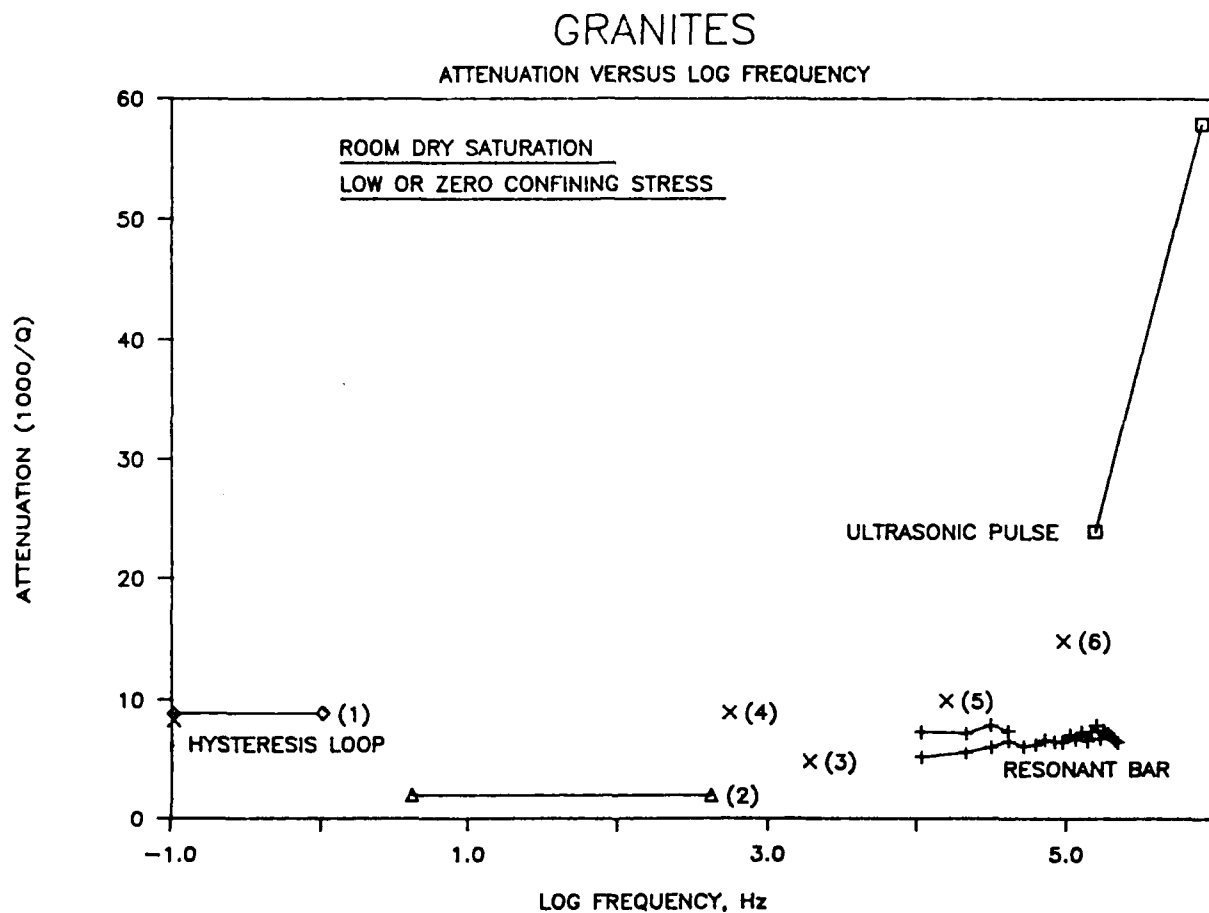


Figure 9. Experimental attenuation measurements versus log frequency for dry granite. Hysteresis loop, resonant bar, and ultrasonic pulse results are labelled. Other results: (1) Liu and Peselnick, 1983; (2) Spencer, 1981; (3) Winkler et al., 1979; (4) Tittmann, 1984; (5) Johnston and Toksoz, 1980; (6) Gordon and Davis, 1968

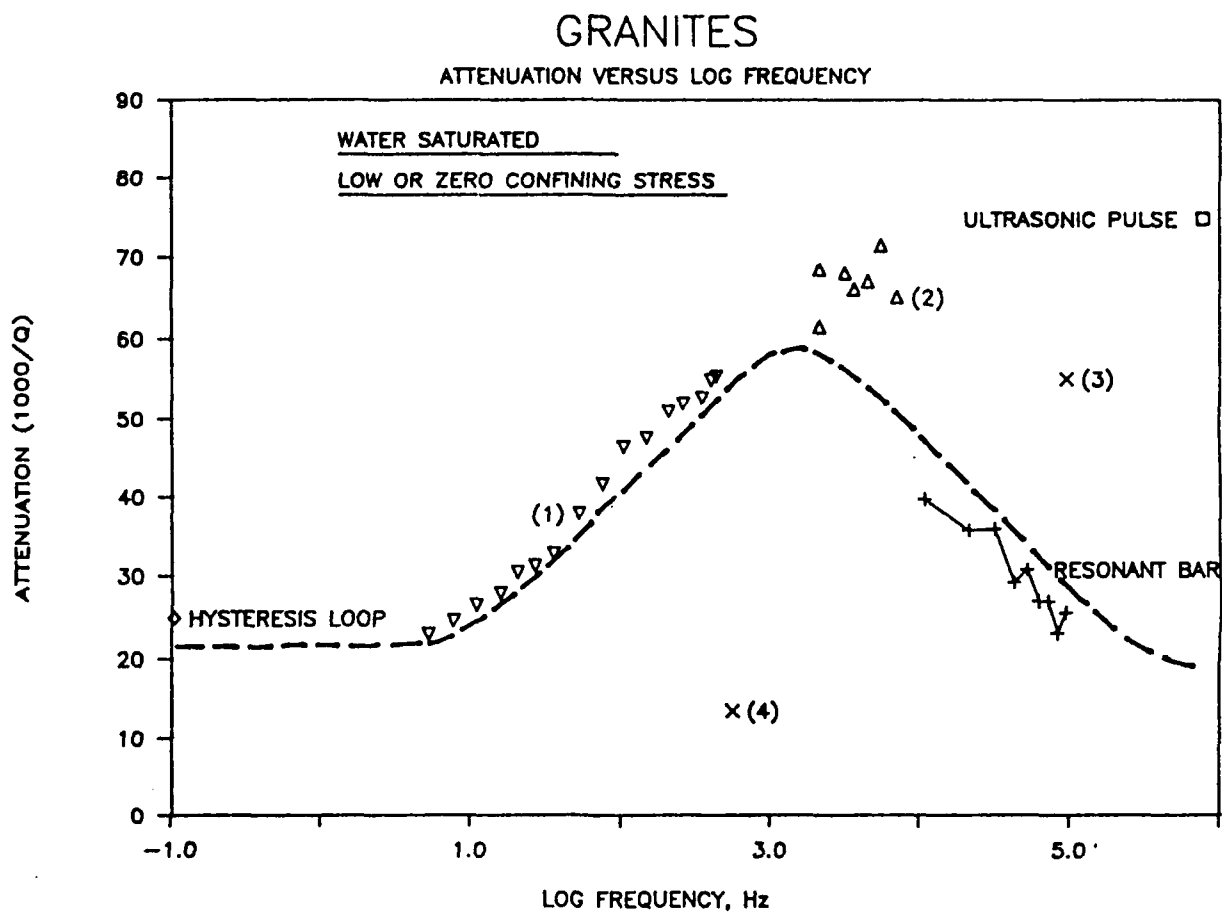


Figure 10. Experimental attenuation measurements versus log frequency for water saturated granites. Hysteresis loop, resonant bar, and ultrasonic pulse results are labelled. Other results: (1) Spencer, 1981; (2) Murphy, 1984; (3) Gordon and Davis, 1968; (4) Tittmann, 1984;

Prof. Thomas Ahrens
Seismological Lab, 252-21
Division of Geological & Planetary Sciences
California Institute of Technology
Pasadena, CA 91125

Prof. Charles B. Archambeau
CIRES
University of Colorado
Boulder, CO 80309

Prof. Muawia Barazangi
Institute for the Study of the Continent
Cornell University
Ithaca, NY 14853

Dr. Douglas R. Baumgardt
ENSCO, Inc
5400 Port Royal Road
Springfield, VA 22151-2388

Prof. Jonathan Berger
IGPP, A-025
Scripps Institution of Oceanography
University of California, San Diego
La Jolla, CA 92093

Dr. Lawrence J. Burdick
Woodward-Clyde Consultants
566 El Dorado Street
Pasadena, CA 91109-3245

Dr. Karl Coyner
New England Research, Inc.
76 Olcott Drive
White River Junction, VT 05001

Prof. Vernon F. Cormier
Department of Geology & Geophysics
U-45, Room 207
The University of Connecticut
Storrs, CT 06268

Prof. Steven Day
Department of Geological Sciences
San Diego State University
San Diego, CA 92182

Dr. Zoltan A. Der
ENSCO, Inc.
5400 Port Royal Road
Springfield, VA 22151-2388

Prof. John Ferguson
Center for Lithospheric Studies
The University of Texas at Dallas
P.O. Box 830688
Richardson, TX 75083-0688

Prof. Stanley Flatte
Applied Sciences Building
University of California
Santa Cruz, CA 95064

Dr. Alexander Florence
SRI International
333 Ravenswood Avenue
Menlo Park, CA 94025-3493

Prof. Henry L. Gray
Vice Provost and Dean
Department of Statistical Sciences
Southern Methodist University
Dallas, TX 75275

Dr. Indra Gupta
Teledyne Geotech
314 Montgomery Street
Alexandria, VA 22314

Prof. David G. Harkrider
Seismological Laboratory
Division of Geological & Planetary Sciences
California Institute of Technology
Pasadena, CA 91125

Prof. Donald V. Helmberger
Seismological Laboratory
Division of Geological & Planetary Sciences
California Institute of Technology
Pasadena, CA 91125

Prof. Eugene Herrin
Institute for the Study of Earth and Man
Geophysical Laboratory
Southern Methodist University
Dallas, TX 75275

Prof. Robert B. Herrmann
Department of Earth & Atmospheric Sciences
St. Louis University
St. Louis, MO 63156

Prof. Bryan Isacks
Cornell University
Department of Geological Sciences
SNEE Hall
Ithaca, NY 14850

Dr. Rong-Song Jih
Teledyne Geotech
314 Montgomery Street
Alexandria, VA 22314

Prof. Lane R. Johnson
Seismographic Station
University of California
Berkeley, CA 94720

Prof. Alan Kafka
Department of Geology & Geophysics
Boston College
Chestnut Hill, MA 02167

Prof. Fred K. Lamb
University of Illinois at Urbana-Champaign
Department of Physics
1110 West Green Street
Urbana, IL 61801

Prof. Charles A. Langston
Geosciences Department
403 Deike Building
The Pennsylvania State University
University Park, PA 16802

Professor Thorne Lay
Institute of Tectonics
Earth Science Board
University of California, Santa Cruz
Santa Cruz, CA 95064

Prof. Arthur Lerner-Lam
Lamont-Doherty Geological Observatory
of Columbia University
Palisades, NY 10964

Dr. Christopher Lynnes
Teledyne Geotech
314 Montgomery Street
Alexandria, VA 22314

Prof. Peter Malin
University of California at Santa Barbara
Institute for Crustal Studies
Santa Barbara, CA 93106

Dr. Randolph Martin, III
New England Research, Inc.
76 Olcott Drive
White River Junction, VT 05001

Dr. Gary McCartor
Mission Research Corporation
735 State Street
P.O. Drawer 719
Santa Barbara, CA 93102 (2 copies)

Prof. Thomas V. McEvilly
Seismographic Station
University of California
Berkeley, CA 94720

Dr. Keith L. McLaughlin
S-CUBED
A Division of Maxwell Laboratory
P.O. Box 1620
La Jolla, CA 92038-1620

Prof. William Menke
Lamont-Doherty Geological Observatory
of Columbia University
Palisades, NY 10964

Stephen Miller
SRI International
333 Ravenswood Avenue
Box AF 116
Menlo Park, CA 94025-3493

Prof. Bernard Minster
IGPP, A-025
Scripps Institute of Oceanography
University of California, San Diego
La Jolla, CA 92093

Prof. Brian J. Mitchell
Department of Earth & Atmospheric Sciences
St. Louis University
St. Louis, MO 63156

Mr. Jack Murphy
S-CUBED, A Division of Maxwell Laboratory
11800 Sunrise Valley Drive
Suite 1212
Reston, VA 22091 (2 copies)

Dr. Bao Nguyen
GL/LWH
Hanscom AFB, MA 01731-5000

Prof. John A. Orcutt
IGPP, A-025
Scripps Institute of Oceanography
University of California, San Diego
La Jolla, CA 92093

Prof. Keith Priestley
University of Nevada
Mackay School of Mines
Reno, NV 89557

Prof. Paul G. Richards
Lamont-Doherty Geological Observatory
of Columbia University
Palisades, NY 10964

Dr. Wilmer Rivers
Teledyne Geotech
314 Montgomery Street
Alexandria, VA 22314

Dr. Alan S. Ryali, Jr.
Center for Seismic Studies
1300 North 17th Street
Suite 1450
Arlington, VA 22209-2308

Prof. Charles G. Sammis
Center for Earth Sciences
University of Southern California
University Park
Los Angeles, CA 90089-0741

Prof. Christopher H. Scholz
Lamont-Doherty Geological Observatory
of Columbia University
Palisades, NY 10964

Prof. David G. Simpson
Lamont-Doherty Geological Observatory
of Columbia University
Palisades, NY 10964

Dr. Jeffrey Stevens
S-CUBED
A Division of Maxwell Laboratory
P.O. Box 1620
La Jolla, CA 92038-1620

Prof. Brian Stump
Institute for the Study of Earth & Man
Geophysical Laboratory
Southern Methodist University
Dallas, TX 75275

Prof. Jeremiah Sullivan
University of Illinois at Urbana-Champaign
Department of Physics
1110 West Green Street
Urbana, IL 61801

Prof. Clifford Thurber
University of Wisconsin-Madison
Department of Geology & Geophysics
1215 West Dayton Street
Madison, WS 53706

Prof. M. Nafi Toksoz
Earth Resources Lab
Massachusetts Institute of Technology
42 Carleton Street
Cambridge, MA 02142

Prof. John E. Vidale
University of California at Santa Cruz
Seismological Laboratory
Santa Cruz, CA 95064

Prof. Terry C. Wallace
Department of Geosciences
Building #77
University of Arizona
Tucson, AZ 85721

Dr. Raymond Willeman
GL/LWH
Hanscom AFB, MA 01731-5000

Dr. Lorraine Wolf
GL/LWH
Hanscom AFB, MA 01731-5000

Prof. Francis T. Wu
Department of Geological Sciences
State University of New York
at Binghamton
Vestal, NY 13901

OTHERS (United States)

Dr. Monem Abdel-Gawad
Rockwell International Science Center
1049 Camino Dos Rios
Thousand Oaks, CA 91360

Prof. Keiiti Aki
Center for Earth Sciences
University of Southern California
University Park
Los Angeles, CA 90089-0741

Prof. Shelton S. Alexander
Geosciences Department
403 Deike Building
The Pennsylvania State University
University Park, PA 16802

Dr. Kenneth Anderson
BBNSTC
Mail Stop 14/1B
Cambridge, MA 02238

Dr. Ralph Archuleta
Department of Geological Sciences
University of California at Santa Barbara
Santa Barbara, CA 93102

Dr. Thomas C. Bache, Jr.
Science Applications Int'l Corp.
10210 Campus Point Drive
San Diego, CA 92121 (2 copies)

J. Barker
Department of Geological Sciences
State University of New York
at Binghamton
Vestal, NY 13901

Dr. T.J. Bennett
S-CUBED
A Division of Maxwell Laboratory
11800 Sunrise Valley Drive, Suite 1212
Reston, VA 22091

Mr. William J. Best
907 Westwood Drive
Vienna, VA 22180

Dr. N. Biswas
Geophysical Institute
University of Alaska
Fairbanks, AK 99701

Dr. G.A. Bollinger
Department of Geological Sciences
Virginia Polytechnical Institute
21044 Derring Hall
Blacksburg, VA 24061

Dr. Stephen Bratt
Science Applications Int'l Corp.
10210 Campus Point Drive
San Diego, CA 92121

Michael Browne
Teledyne Geotech
3401 Shiloh Road
Garland, TX 75041

Mr. Roy Burger
1221 Serry Road
Schenectady, NY 12309

Dr. Robert Burrige
Schlumberger-Doll Research Center
Old Quarry Road
Ridgefield, CT 06877

Dr. Jerry Carter
Rondout Associates
P.O. Box 224
Stone Ridge, NY 12484

Dr. W. Winston Chan
Teledyne Geotech
314 Montgomery Street
Alexandria, VA 22314-1581

Dr. Theodore Cherry
Science Horizons, Inc.
710 Encinitas Blvd., Suite 200
Encinitas, CA 92024 (2 copies)

Prof. Jon F. Claerbout
Department of Geophysics
Stanford University
Stanford, CA 94305

Prof. Robert W. Clayton
Seismological Laboratory
Division of Geological & Planetary Sciences
California Institute of Technology
Pasadena, CA 91125

Prof. F. A. Dahlen
Geological and Geophysical Sciences
Princeton University
Princeton, NJ 08544-0636

Dr. Jeffrey W. Given
Sierra Geophysics
11255 Kirkland Way
Kirkland, WA 98033

Prof. Anton W. Dainty
Earth Resources Lab
Massachusetts Institute of Technology
42 Carleton Street
Cambridge, MA 02142

Prof. Stephen Grand
University of Texas at Austin
Department of Geological Sciences
Austin, TX 78713-7909

Prof. Adam Dziewonski
Hoffman Laboratory
Harvard University
20 Oxford St
Cambridge, MA 02138

Prof. Roy Greenfield
Geosciences Department
403 Deike Building
The Pennsylvania State University
University Park, PA 16802

Prof. John Ebel
Department of Geology & Geophysics
Boston College
Chestnut Hill, MA 02167

Dan N. Hagedorn
Battelle
Pacific Northwest Laboratories
Battelle Boulevard
Richland, WA 99352

Eric Fielding
SNEE Hall
INSTOC
Cornell University
Ithaca, NY 14853

Kevin Hutchenson
Department of Earth Sciences
St. Louis University
3507 Laclede
St. Louis, MO 63103

Prof. Donald Forsyth
Department of Geological Sciences
Brown University
Providence, RI 02912

Prof. Thomas H. Jordan
Department of Earth, Atmospheric
and Planetary Sciences
Massachusetts Institute of Technology
Cambridge, MA 02139

Prof. Art Frankel
Mail Stop 922
Geological Survey
790 National Center
Reston, VA 22092

Robert C. Kemerait
ENSCO, Inc.
445 Pineda Court
Melbourne, FL 32940

Dr. Anthony Gangi
Texas A&M University
Department of Geophysics
College Station, TX 77843

William Kikendall
Teledyne Geotech
3401 Shiloh Road
Garland, TX 75041

Dr. Freeman Gilbert
Inst. of Geophysics & Planetary Physics
University of California, San Diego
P.O. Box 109
La Jolla, CA 92037

Prof. Leon Knopoff
University of California
Institute of Geophysics & Planetary Physics
Los Angeles, CA 90024

Mr. Edward Giller
Pacific Sierra Research Corp.
1401 Wilson Boulevard
Arlington, VA 22209

Prof. L. Timothy Long
School of Geophysical Sciences
Georgia Institute of Technology
Atlanta, GA 30332

Prof. Art McGarr
Mail Stop 977
Geological Survey
345 Middlefield Rd.
Menlo Park, CA 94025

Dr. George Mellman
Sierra Geophysics
11255 Kirkland Way
Kirkland, WA 98033

Prof. John Nabelek
College of Oceanography
Oregon State University
Corvallis, OR 97331

Prof. Geza Nagy
University of California, San Diego
Department of Ames, M.S. B-010
La Jolla, CA 92093

Prof. Amos Nur
Department of Geophysics
Stanford University
Stanford, CA 94305

Prof. Jack Oliver
Department of Geology
Cornell University
Ithaca, NY 14850

Prof. Robert Phinney
Geological & Geophysical Sciences
Princeton University
Princeton, NJ 08544-0636

Dr. Paul Pomeroy
Rondout Associates
P.O. Box 224
Stone Ridge, NY 12484

Dr. Jay Pulli
RADIX System, Inc.
2 Taft Court, Suite 203
Rockville, MD 20850

Dr. Norton Rimer
S-CUBED
A Division of Maxwell Laboratory
P.O. Box 1620
La Jolla, CA 92038-1620

Prof. Larry J. Ruff
Department of Geological Sciences
1006 C.C. Little Building
University of Michigan
Ann Arbor, MI 48109-1063

Dr. Richard Sailor
TASC Inc.
55 Walkers Brook Drive
Reading, MA 01867

Thomas J. Sereno, Jr.
Science Application Int'l Corp.
10210 Campus Point Drive
San Diego, CA 92121

John Sherwin
Teledyne Geotech
3401 Shiloh Road
Garland, TX 75041

Prof. Robert Smith
Department of Geophysics
University of Utah
1400 East 2nd South
Salt Lake City, UT 84112

Prof. S. W. Smith
Geophysics Program
University of Washington
Seattle, WA 98195

Dr. Stewart Smith
IRIS Inc.
1616 North Fort Myer Drive
Suite 1440
Arlington, VA 22209

Dr. George Sutton
Rondout Associates
P.O. Box 224
Stone Ridge, NY 12484

Prof. L. Sykes
Lamont-Doherty Geological Observatory
of Columbia University
Palisades, NY 10964

Prof. Pradeep Talwani
Department of Geological Sciences
University of South Carolina
Columbia, SC 29208

Prof. Ta-liang Teng
Center for Earth Sciences
University of Southern California
University Park
Los Angeles, CA 90089-0741

- Dr. R.B. Tittmann
Rockwell International Science Center
1049 Camino Dos Rios
P.O. Box 1085
Thousand Oaks, CA 91360

Dr. Gregory van der Vink
IRIS, Inc.
1616 North Fort Myer Drive
Suite 1440
Arlington, VA 22209

William R. Walter
Seismological Laboratory
University of Nevada
Reno, NV 89557

Dr. Gregory Wojcik
Weidlinger Associates
4410 El Camino Real
Suite 110
Los Altos, CA 94022

Prof. John H. Woodhouse
Hoffman Laboratory
Harvard University
20 Oxford Street
Cambridge, MA 02138

Dr. Gregory B. Young
ENSCO, Inc.
5400 Port Royal Road
Springfield, VA 22151-2388

GOVERNMENT

Dr. Ralph Alewine III
DARPA/NMRO
1400 Wilson Boulevard
Arlington, VA 01731-5000

Mr. James C. Battis
GL/LWH
Hanscom AFB, MA 22209-2308

Dr. Robert Blandford
DARPA/NMRO
1400 Wilson Boulevard
Arlington, VA 87185

Eric Chael
Division 9241
Sandia Laboratory
Albuquerque, NM 01731-5000

Dr. John J. Cipar
GL/LWH
Hanscom AFB, MA 01731-5000

Mr. Jeff Duncan
Office of Congressman Markey
2133 Rayburn House Bldg.
Washington, D.C. 20515

Dr. Jack Evernden
USGS - Earthquake Studies
345 Middlefield Road
Menlo Park, CA 94025

Art Frankel
USGS
922 National Center
Reston, VA 22092

Dr. T. Hanks
USGS
Nat'l Earthquake Research Center
345 Middlefield Road
Menlo Park, CA 94025

Dr. James Hannon
Lawrence Livermore Nat'l Laboratory
P.O. Box 808
Livermore, CA 94550

Paul Johnson
ESS-4, Mail Stop J979
Los Alamos National Laboratory
Los Alamos, NM 87545

Janet Johnston
GL/LWH
Hanscom AFB, MA 01731-5000

Dr. Katharine Kadinsky-Cade
GL/LWH
Hanscom AFB, MA 01731-5000

Ms. Ann Kerr
IGPP, A-025
Scripps Institute of Oceanography
University of California, San Diego
La Jolla, CA 92093

Dr. Max Koontz
US Dept of Energy/DP 5
Forrestal Building
1000 Independence Avenue
Washington, DC 20585

Dr. W.H.K. Lee
Office of Earthquakes, Volcanoes,
& Engineering
345 Middlefield Road
Menlo Park, CA 94025

Dr. William Leith
U.S. Geological Survey
Mail Stop 928
Reston, VA 22092

Dr. Richard Lewis
Director, Earthquake Engineering & Geophysics
U.S. Army Corps of Engineers
Box 631
Vicksburg, MS 39180

James F. Lewkowicz
GL/LWH
Hanscom AFB, MA 01731-5000

Mr. Alfred Lieberman
ACDA/VI-OA'State Department Bldg
Room 5726
320 - 21st Street, NW
Washington, DC 20451

Stephen Mangino
GL/LWH
Hanscom AFB, MA 01731-5000

Dr. Frank F. Pilotte
HQ AFTAC/TT
Patrick AFB, FL 32925-6001

Dr. Robert Masse
Box 25046, Mail Stop 967
Denver Federal Center
Denver, CO 80225

Katie Poley
CIA-OSWR/NED
Washington, DC 20505

Art McGarr
U.S. Geological Survey, MS-977
345 Middlefield Road
Menlo Park, CA 94025

Mr. Jack Rachlin
U.S. Geological Survey
Geology, Rm 3 C136
Mail Stop 928 National Center
Reston, VA 22092

Richard Morrow
ACDA/VI, Room 5741
320 21st Street N.W.
Washington, DC 20451

Dr. Robert Reinke
WL/NTESG
Kirtland AFB, NM 87117-6008

Dr. Keith K. Nakanishi
Lawrence Livermore National Laboratory
P.O. Box 808, L-205
Livermore, CA 94550

Dr. Byron Ristvet
HQ DNA, Nevada Operations Office
Attn: NVCG
P.O. Box 98539
Las Vegas, NV 89193

Dr. Carl Newton
Los Alamos National Laboratory
P.O. Box 1663
Mail Stop C335, Group ESS-3
Los Alamos, NM 87545

Dr. George Rothe
HQ AFTAC/TGR
Patrick AFB, FL 32925-6001

Dr. Kenneth H. Olsen
Los Alamos Scientific Laboratory
P.O. Box 1663
Mail Stop C335, Group ESS-3
Los Alamos, NM 87545

Dr. Michael Shore
Defense Nuclear Agency/SPSS
6801 Telegraph Road
Alexandria, VA 22310

Howard J. Patton
Lawrence Livermore National Laboratory
P.O. Box 808, L-205
Livermore, CA 94550

Donald L. Springer
Lawrence Livermore National Laboratory
P.O. Box 808, L-205
Livermore, CA 94550

Mr. Chris Paine
Office of Senator Kennedy, SR 315

Dr. Lawrence Turnbull
OSWR/NED
Central Intelligence Agency, Room 5G48
Washington, DC 20505

United States Senate
Washington, DC 20510

Colonel Jerry J. Perrizo
AFOSR/NP, Building 410
Bolling AFB
Washington, DC 20332-6448

Dr. Thomas Weaver
Los Alamos National Laboratory
P.O. Box 1663, Mail Stop C335
Los Alamos, NM 87545

J.J. Zucca
Lawrence Livermore National Laboratory
Box 808
Livermore, CA 94550

Defense Technical Information Center
Cameron Station
Alexandria, VA 22314 (5 copies)

GL/SULL
Research Library
Hanscom AFB, MA 01731-5000 (2 copies)

Defense Intelligence Agency
Directorate for Scientific &
Technical Intelligence
Washington, DC 20301

Secretary of the Air Force (SAFRD)
Washington, DC 20330

AFTAC/CA
(STINFO)
Patrick AFB, FL 32925-6001

Office of the Secretary Defense
DDR & E
Washington, DC 20330

TACTEC
Battelle Memorial Institute
505 King Avenue
Columbus, OH 43201 (Final Report Only)

HQ DNA
Attn: Technical Library
Washington, DC 20305

Mr. Charles L. Taylor
GL/LWH

Hanscom AFB, MA 01731-5000

DARPA/RMO/RETRIEVAL
1400 Wilson Boulevard
Arlington, VA 22209

DARPA/RMO/Security Office
1400 Wilson Boulevard
Arlington, VA 22209

Geophysics Laboratory
Attn: XO
Hanscom AFB, MA 01731-5000

Geophysics Laboratory
Attn: LW
Hanscom AFB, MA 01731-5000

DARPA/PM
1400 Wilson Boulevard
Arlington, VA 22209

CONTRACTORS (Foreign)

Dr. Ramon Cabre, S.J.
Observatorio San Calixto
Casilla 5939
La Paz, Bolivia

Prof. Hans-Peter Harjes
Institute for Geophysik
Ruhr University/Bochum
P.O. Box 102148
4630 Bochum 1, FRG

Prof. Eystein Husebye
NTNF/NORSAR
P.O. Box 51
N-2007 Kjeller, NORWAY

Prof. Brian L.N. Kennett
Research School of Earth Sciences
Institute of Advanced Studies
G.P.O. Box 4
Canberra 2601, AUSTRALIA

Dr. Bernard Massinon
Societe Radiomana
27 rue Claude Bernard
75005 Paris, FRANCE (2 Copies)

Dr. Pierre Mecheler
Societe Radiomana
27 rue Claude Bernard
75005 Paris, FRANCE

Dr. Svein Mykkeltveit
NTNF/NORSAR
P.O. Box 51
N-2007 Kjeller, NORWAY

FOREIGN (Others)

Dr. Peter Basham
Earth Physics Branch
Geological Survey of Canada
1 Observatory Crescent
Ottawa, Ontario, CANADA K1A 0Y3

Dr. Eduard Berg
Institute of Geophysics
University of Hawaii
Honolulu, HI 96822

Dr. Michel Bouchon
I.R.I.G.M.-B.P. 68
38402 St. Martin D'Herès
Cedex, FRANCE

Dr. Hilmar Bungum
NTNF/NORSAR
P.O. Box 51
N-2007 Kjeller, NORWAY

Dr. Michel Campillo
Observatoire de Grenoble
I.R.I.G.M.-B.P. 53
38041 Grenoble, FRANCE

Dr. Kin Yip Chun
Geophysics Division
Physics Department
University of Toronto
Ontario, CANADA M5S 1A7

Dr. Alan Douglas
Ministry of Defense
Blacknest, Brimpton
Reading RG7-4RS, UNITED KINGDOM

Dr. Roger Hansen
NTNF/NORSAR
P.O. Box 51
N-2007 Kjeller, NORWAY

Dr. Manfred Henger
Federal Institute for Geosciences & Nat'l Res.
Postfach 510153
D-3000 Hanover 51, FRG

Ms. Eva Johannisson
Senior Research Officer
National Defense Research Inst.
P.O. Box 27322
S-102 54 Stockholm, SWEDEN

Dr. Fekadu Kebede
Seismological Section
Box 12019
S-750 Uppsala, SWEDEN

Dr. Tormod Kvaerna
NTNF/NORSAR
P.O. Box 51
N-2007 Kjeller, NORWAY

Dr. Peter Marshal
Procurement Executive
Ministry of Defense
Blacknest, Brimpton
Reading FG7-4RS, UNITED KINGDOM

Prof. Ari Ben-Menahem
Department of Applied Mathematics
Weizman Institute of Science
Rehovot, ISRAEL 951729

Dr. Robert North
Geophysics Division
Geological Survey of Canada
1 Observatory Crescent
Ottawa, Ontario, CANADA K1A 0Y3

Dr. Frode Ringdal
NTNF/NORSAR
P.O. Box 51
N-2007 Kjeller, NORWAY

Dr. Jorg Schlittenhardt
Federal Institute for Geosciences & Nat'l Res.
Postfach 510153
D-3000 Hannover 51, FEDERAL REPUBLIC OF
GERMANY

Prof. Daniel Walker
University of Hawaii
Institute of Geophysics
Honolulu, HI 96822